

**REVIEW OF AERONAUTICAL FATIGUE
INVESTIGATIONS IN JAPAN
DURING THE PERIOD JUNE 2009 TO MAY 2011**

Edited by

Nobuo Takeda
The University of Tokyo

For Presentation at the 32nd Conference of
the International Committee on Aeronautical Fatigue

Montreal, Canada, 29-31 May 2011

Contents

| | page |
|---|------|
| 1. INTRODUCTION | 4 |
| 2. FATIGUE IN METALLIC MATERIALS AND COMPONENTS | 5 |
| 2.1 Evaluation of Fatigue Crack Growth Behavior in FSW Joint by Experiment, Analysis and Elasto-Plastic FEM | 5 |
| 2.2 Mechanical Property of Friction Stir Welded Butt Joint in 2 mm Thick Aluminum Alloy | 7 |
| 2.3 The effect of Fine Particle Shot Peening on the fatigue properties of 7050-T7451 | 9 |
| 2.4 Development of High Strength and Excellent Extrudability Aluminum Alloy 2013 Extrusion for Aircraft Structures | 10 |
| 2.5 Fatigue and Impact Damage of Magnesium-Lithium Based Fiber Metal Laminates | 11 |
| 2.6 Critical Distance for Fatigue Life Prediction in Aerospace Materials | 13 |
| 3. FATIGUE IN COMPOSITE MATERIALS AND COMPONENTS | 14 |
| 3.1 Damage Tolerance Demonstration of Flange Joint for Aero Engine Composite Fan Case | 14 |
| 3.2 Multiaxial Damage Modeling of Bearing Failure in CFRP Bolted Joints Based on Fiber Compressive Failure Criterion | 16 |
| 4. STRUCTURAL HEALTH MONITORING | 17 |
| 4.1 Memorization and Detection of an Arrested Crack in a Foam-core Sandwich Structures Using Embedded Metal Wires and Fiber-optic Sensors | 17 |
| 4.2 Damage Detection of CFRP Bolted Joints Using Embedded Optical Fibers with BOCDA System | 18 |
| 4.3 Full-Field Damage Detection System for Scarf Repaired Composite Structures Using Pulse-Laser Generated Lamb Waves | 19 |
| 5. LIFE EVALUATION ANALYSIS | 19 |
| 5.1 A structural Defect Expansion Model Based on Physical Correlation | 19 |

| | |
|--|----|
| 6. FULL-SCALE TESTING | 21 |
| 6.1 XP-1/XC-2 Full Scale Strength Test | 21 |
| 6.2 Durability and Damage Tolerance Evaluation of VaRTM Composite Wing Structure | 22 |
| 7 AIRCRAFT ACCIDENT INVESTIGATION | 23 |
| 7.1 Aircraft Accident Investigation and Aircraft Serious Incident Investigation | 23 |
| ACKNOWLEDGEMENTS | 25 |
| TABLES AND FIGURES | 26 |

(Last Page 55)

1. INTRODUCTION

Nobuo Takeda, National Delegate, The University of Tokyo

This review summarizes the papers on the study of aeronautical fatigue and related topics conducted in Japan during June 2009 to May 2011.

The papers were contributed by following organizations:

Japan Aerospace Exploration Agency (JAXA)
 Japan Aerospace Technology Foundation (JAST)
 Technical Research and Development Institute (TRDI), MOD
 Japan Transport Safety Board (JTSB)
 Mitsubishi Heavy Industries, Ltd. (MHI)
 Kawasaki Heavy Industries, Ltd. (KHI)
 Fuji Heavy Industries, Ltd. (FHI)
 IHI Corporations
 IHI Aerospace Co. Ltd.
 Sumitomo Light Metal Industries, Ltd.
 The University of Tokyo
 Tohoku University
 Waseda University

The general activities on aircraft development program in Japan during 2009 to 2011 is summarized as follows:

- The development of MRJ (Mitsubishi Regional Jet, 70- to 90-seat regional jets) aircraft is progressing on schedule. The production started at Mitsubishi Aircraft Corporation in Nagoya. The maiden flight is expected in 2012 and the first service flight in 2014.
- Both XP-1, the 4 turbo-fan mid-size maritime patrol airplane and XC-2, the twin turbo-fan large-size cargo transport airplane, have been subject to the final tests including full-scale static test and full scale fatigue test. Both XP-1 and XC-2 made the first flight in September, 2007 and in January, 2010, respectively.
- “Civil Aviation Fundamental Technology Program -Advanced Materials & Process Development for Next-Generation Aircraft Structures” (FY2008-2012) is being conducted at the Materials Process Technology

Center, in collaboration with industries, universities and national laboratories. The program includes two projects on (1) Composite Structure Health Monitoring and Diagnosis, and (2) Material Development and Processing of Next-Generation Titanium Alloy Structural Members.

2. FATIGUE IN METALLIC MATERIALS AND COMPONENTS

2.1 Evaluation of Fatigue Crack Growth Behavior in FSW Joint by Experiment, Analysis and Elasto-Plastic FEM

T. Okada¹, K. Kuwayama², M. Asakawa², T. Nakamura¹, S. Machida¹, S. Fujita², T. Noguchi², and H. Terada³

¹ Aviation Program Group, Japan Aerospace Exploration Agency (JAXA), Tokyo, Japan

² Waseda University, Tokyo, Japan;

³ Japan Aerospace Technology Foundation, Tokyo, Japan;

Friction stir welding (FSW) is one of the new weld processes developed in recent years. It has the capability to welding high strength aluminum alloys. From a point of reducing the cost and weight, FSW is expected to be applied to the primary structure of aircraft. However, to comply with damage tolerance requirement, it is important for friction stir welded structure to investigate the relationship between the fatigue crack growth property of a panel and the residual stress in and around the weld line. Then many research activities focuses on these issues^{1,2}). In ICAF2009, authors presented fatigue crack growth test result of FSW panel joined by 2024-T3 aluminum alloy and evaluated the effects of residual stress on crack growth rate and the effect of inclined angel of weld line on crack growth rate and direction of crack growth. Several approaches exist to predict fatigue crack growth behavior in residual stress field. One of the procedure is based on the crack closure concept, which evaluates the crack opening stress or the stress intensity factor for the crack opening stress³). Another approach uses the correction factor for stress intensity factor to take into account for the effect of residual stress field⁴).

Following two parameters, distance between the weld line and the center of the crack starter and magnitude of tensile residual stress, are evaluated by the

elasto-plastic FEM for their effect on the crack opening stress. The analysis considers the effect of residual stress and external stress on plastic deformation around the crack and on the crack opening stress (Fig.1). FEM results indicate that the calculated crack opening stress of FSW panel decreases at and around the welding line and asymptotically reaches to the opening stress of the base material. And the crack opening stress when the crack tip is within the welding line decreases with the increase of distance between weld line and the center of the notch (Fig.2). The magnitude of peak residual stress is set to 295, 250 or 115MPa and its effect on the crack opening stress are also evaluated. The results indicates that the crack opening stress for the FSW plate nonlinearly decreases with the increase of the peak residual stress and its reduction gets slow as the increase of the residual stress.

The $da/dN-\Delta K$ curves for FSW plate are numerically obtained by using experimental $da/dN-\Delta K$ curve for base material and the calculated crack opening stress (Fig.3). The a-N curves are also obtained by integrating the $da/dN-\Delta K$ curves. These obtained curves agree to the experimental result. On the other hand, the $da/dN-\Delta K$ curves where ΔK is evaluated by correction factor relatively correspond to the test result, while the calculated a-N curves do not coincide well to the test results. It is because the difference between the calculated crack growth rate and the experimental growth rate is apparent in case the crack tip is in the compressive residual stress field.

These results indicate that the crack opening stress of the FSW panel is adequately evaluated by the elasto-plastic FEM. And by using calculated crack opening stress, the $da/dN-\Delta K$ curves and the a-N curves for FSW panel could be predicted reasonably.

References

- 1) Irving P., Ma Y.E., Zhang X., Servetti G., Williams S., Moore G., dos Santos J., Pacchione M.: Control of Crack Growth Rates and Crack Trajectories for Enhanced Fail Safety and Damage Tolerance in Welded Aircraft Structures, Proceedings of the 25th International Symposium on Aeronautical Fatigue, 27-29 May 2009, Rotterdam, Netherland, pp. 387-405.
- 2) Lemmen H.J.K., Alderliesten R.C., Benedictus R.: Detailed Strain Field Analyses of Fatigue Cracks in Friction Stir Welded Joints, Proceedings of the 25th

International Symposium on Aeronautical Fatigue, 27-29 May 2009, Rotterdam, Netherland, pp. 619-642.

3) Dalle-Donne C., Lima E., Wegener J., Pyzalla A., Buslaps, T.: Investigation of Residual Stress in Friction Stir Welds, Proceedings of the 3rd International FSW Symposium, 2001, TWI Ltd.

4) Terada, H., An Analysis of a Crack in the Residual Stress Field of Welding: Role of Fracture Mechanics in Modern Technology, 1987, pp. 899-910, Elsevier Science Publishers B.V.

2.2 Mechanical Property of Friction Stir Welded Butt Joint in 2 mm Thick Aluminum Alloy

Takao Okada and Shigeru Machida

Aviation Program Group, Japan Aerospace Exploration Agency (JAXA)

For commercial aircraft, FSW is firstly applied to normal category aircraft in 2006 and its application to transport category aircraft is planned by some companies. Therefore FSW structure used to the aircraft structure needs to comply with the necessary requirement such as fatigue, damage tolerance and etc. and the intensive research activities have been conducted¹⁻³⁾. But many of the FSW research use a plate thickness of 6mm or more. It is thicker than that for many aircraft structures such as a fuselage and a wing skin. And the property of FSW is affected by welding condition. In this research, two sizes of weld tool are used to prepare friction stir welded butt joint of 2024-T3 Aluminum alloy of 2mm thickness and their mechanical properties are evaluated. Mechanical property for base material is obtained to compare those for FSW. Tests are conducted based on corresponding ASTM standards.

Indentation hardness distribution in the welding area is measured by the micro indentation hardness test procedure (ASTM E-384) to evaluate the possibility to predict probable crack nucleation sites of the joint. Test results revealed that, irrespective to welding condition, typical hardness reduction is not necessarily observed on the section of the welding line (Fig. 4). This result is different from that for thicker FSW plate obtained by other research.

Static tests result indicate the yield stress for FSW joint is equal or a little higher than that for base material, while its ultimate strength is about 10 % lower

than that for base material. The coefficient of variance is low irrespective to specimen types. Fracture surface observation shows that the fracture origin is the Lack of Penetration (LOP) for one specimen type. By removing the LOP, the ultimate strength of the FSW joint closes to that of the base material. In case the LOP is not fracture origin, its fracture feature is same as that for base material.

Fatigue test results (Fig.5) indicated the several types of fatigue fracture origin such as LOP, burr, tool mark and etc. are observed. LOP could be a fatigue crack origin for the FSW specimen in case its static fracture origin could be LOP. The size of weld tool affects the size of the tool mark and the burr of the FSW and it apparently affects the fracture origin and the fatigue life. Because the LOP, the tool mark and the burr exists along the welding line, these might cause multiple fracture origin and it might decrease the fatigue life significantly. The size of the burr which could be a fracture origin is compared to that for other paper⁴⁾. The height of the burr was 0.07 mm at most in the case and is smaller than those for our welding cases. The paper concludes that the notch effect induced by the burr is presumably less critical than the thickness reduction at actual fracture site. Therefore, it is supposed that the crack nucleation sites and fatigue life could change significantly if the height of the burrs along the welding line enough increases.

References

- 1) Bussu G., Irving P. E.: The Role of Residual Stress and Heat Affected Zone Properties on Fatigue Crack Propagation in Friction Stir Welded 2024-T351 Aluminum Alloy, *International Journal of Fatigue* 2003, vol. 25, pp. 77-88.
- 2) Lemmen H.J.K., Alderliesten R.C., Homan J.J., Benedictus R.: Fatigue Crack Initiation Behaviour of Friction Stir Welded Joints in Aluminum Alloy, *Proceedings of the 24th International Symposium on Aeronautical Fatigue*, 16-18 May 2007, Naples, Italy, pp. 147-162.
- 3) Sato H., Yamada Y., Tanoue Y. and Sakagawa T.: Fatigue and Crack Propagation Properties of Friction Stir Welded Lap Joint and Panel, *Proceedings of the 23th International Symposium on Aeronautical Fatigue*, 08-10 June 2005, Hamburg, Germany, pp. 645-656.
- 4) Biallas G, Donne CD, Juricic C.: Monotonic and Cyclic Strength of Friction Stir Welded Aluminum Joints. In: Miannay D et. al. *Advances in Mechanical*

Behaviour, Plasticity and Damage: Elsevier science, Kidlington, 2000, pp. 115-120.

2.3 The effect of Fine Particle Shot Peening on the fatigue properties of 7050-T7451

Akiko Inoue

Mitsubishi Heavy Industries, Ltd

Fine Particle Shot Peening (FPSP) was developed in Japan and has been applied in automotive industries such as steel gears and coil springs. For aircraft parts, a fatigue property is an important factor to enhance the durability of structural components. In this study, the fatigue life improvement of 7050-T7451 was achieved by FPSP with glass media of less than 0.1mm in diameter. Fatigue test was performed under the uni-axial loading and the maximum stress was between 275MPa and 413MPa at the stress ratio of 0.1. The fatigue test specimen was round shape with a diameter of 6.35mm at the center of the coupon. An average surface roughness prior to FPSP was 63Ra. The experimental results of the fatigue test are compared with the conventional shot peened (SP) material by steel shot of 0.6mm in diameter and the results are shown in Fig. 6. The fatigue life of FPSP specimens endured more than ten times longer than that of SP specimens, and approximately hundred times longer than the virgin specimens.

SEM images of fractured surfaces are shown in Fig. 7. The fatigue crack initiation sites in a conventional shot peened specimen, or in a virgin specimen, are located on the specimen surface as shown in Fig. 7(b) and (d), while an arrow in Fig. 7(f) indicates that the fatigue crack in the FPSP specimen initiated at the subsurface layer inside of the specimen.

The results of X-ray residual stress measurement are plotted in Fig. 8 from surface to the depth direction. The stress intensity factors at the crack front tip are derived considering the effect of residual stress profiles and the calculated results are plotted in Fig. 9 in relation to the crack size. It shows that the shallow compressive residual stress of FPSP reduces the stress intensity factor, K at the crack tip front, $K_{tip}(FPSP)$ to lower than the threshold, K_{th} . Therefore, the crack initiation from surface is prevented and the fatigue life cycles of FPSP specimens is increased because of a longer crack initiation cycles from subsurface layer. In other words, the effect of fatigue life improvement by FPSP was mainly resulted

from the transition of the crack initiation site from surface to subsurface layer due to a large compressive residual stress layer near the specimen surface.

2.4 Development of High Strength and Excellent Extrudability Aluminum Alloy 2024 Extrusion for Aircraft Structures

Kenichi. Kamimuki*, Etsuko. Yamada*, Hideo. Sano**, Tadashi. Minoda** and Katsuya. Kato**

* Kawasaki Heavy Industries, LTD

** Sumitomo Light Metal Industries, LTD

Aluminum alloy has been used widely for an aircraft structure because of its lightweight. 2024 alloy has high static and high fatigue strength, so it has been applied to the primary structures for half a century. However it has disadvantages of corrosion resistance and formability. On the contrary, the 6000 series have been used for the secondary structures, and their features are excellent corrosion resistance and formability. 6013 has been developed as an alternative alloy to 2024, but 6013-T6 has 20% lower strength than 2024-T3.

Consequently we have improved 6013 alloy and succeeded in the development of alternative alloy, 2013, which has high strength at the same level as 2024. Table 1 shows the chemical compositions of each alloy. In 2013, Cu was increased to improve strength compared to 6013, and Cr was added instead of Mn as a grain-refining element to improve extrudability. Since 2013 has excellent extrudability, it can be extruded to thin complex shapes. Therefore, 2013 can reduce the assembly cost by means of integrated structure. 2013 also has good corrosion resistance because 2013 has the properties of 6000 series, thus it can reduce the maintenance cost. To apply this new alloy as an aircraft material, we have evaluated various properties used as design allowables, and these properties have been registered on Metallic Materials Properties Development & Standardization (MMPDS) which is a public handbook.

Table 2 shows the A values of 2013-T6511 static properties, and the A values of 2024-T3511 in MMPDS for comparison. It shows that the Ft_u of 2013-T6511 is approximately the same as that of 2024-T3511, and other properties of 2013 are 1.2-1.6 times better than those of 2024.

2024 has been widely used as the wing lower panel and the fuselage panel which are loaded repeated tensile load because 2024 has good fatigue properties, and 2024 extrusion has been used as the stringer and cord of the skin panels. To apply widely to the aircraft structure as alternative alloy of 2024, 2013 should have good fatigue properties equal or superior to 2024. The fatigue tests were performed on non-notched specimens ($K_t=1.0$) and notched specimens ($K_t=3.0$) in the longitudinal direction to extrusion. The stress ratios were $R=0.02, 0.3, 0.5$. Figure 10 shows maximum stress-cycles curves of 2013-T6511 and 2024-T3511. The continuous lines in Fig. 10(a) show 2024-T3 data described in MMPDS. $K_t=1.0$ fatigue properties of 2013-T6511 are better than 2024-T3 in high cycle area. Figure 10(b) shows the results of notched fatigue test. 2024-T3511 extrusions were tested under the same conditions with 2013-T6511 ($R=0.02$) for comparison, because the fatigue data ($K_t=3.0$) of 2024-T3 is not described in MMPDS. It is also confirmed that 2013-T6511 has equal fatigue properties in $K_t=3.0$.

Damage tolerance concept is often needed in the important airframe parts that are required fatigue properties, consequently fatigue crack growth test was performed on 2013 and 2024. Figure 11 shows the relationship between fatigue crack growth rate and stress intensity factor for 2013-T6511 and 2024-T3. As shown in Fig. 11, the crack growth rate of 2013-T6511 is equal or smaller than that of 2024-T3 throughout all stress ranges.

A part of this project had been sponsored by The Society of Japanese Aerospace Companies (SJAC).

2.5 Fatigue and Impact Damage of Magnesium-Lithium Based Fiber Metal Laminates

Ayako Oide, Takahiro Nagayama and Atsuhiko Sakabe, Masanori Nakajima and Hiroshi Wakai

Fuji Heavy Industries, Ltd.

Fiber reinforced plastic (FRP) is applied widely to aircraft structure recently for weight reduction. However, it is difficult for FRP to lighten the parts required impact resistance, like leading edge of wing, because it needs to become thick to satisfy requirement of impact resistance.

Then we focused on fiber metal laminates (FML). FML has excellent fatigue capability, good crack growth characteristics under a cyclic load and good impact

resistance compared with monolithic metals. So FML has been gradually used at those areas that are required fatigue and impact on aircraft. But, the density of FML used mainly, like Glare, is 2.4 g/cm^3 that is heavier than that of FRP.

In this work, we made lighter FML, the density is 1.4 g/cm^3 that is lighter than CFRP(1.6 g/cm^3), by using Magnesium-Lithium alloy for metal layer. The paper presents the experimental and the numerical analysis result of the hail impact test for curved Mg-Li FML specimen, and the testing of fatigue test and impact test for Mg-Li FML.

Table 3 shows the experimental and the numerical analysis result of the hail impact test. For this test, the hail 50.8 mm in diameter impacted with the curved specimen that was imitated the leading edge of wing at a speed of 122 m/s. The deformation of the experimental FML specimen was larger than the one of the Aluminum alloy specimen which was tested for comparison. The numerical analysis considered two models, one included the primary delamination and the other neglected the primary delamination. The experimental deformation almost agreed with the one of analysis model with the primary delamination. This result shows that some delamination might occur in the Mg-Li FML specimen of this work, so that the deformation of FML is larger than the one of Aluminum alloy. On the analysis result, the FML specimen without delamination that is 15% lighter than Aluminum alloy specimen showed similar deformation with Aluminum alloy specimen.

A static test results showed the Mg-Li FML had about 30% lower tensile strength compared to Aluminum alloy, but had about 20% higher specific tensile strength compared to Aluminum alloy. The fatigue crack growth test results showed the crack growth speed of FML was faster than the Aluminum alloy and Glare (Fig. 12). To improve the fatigue crack growth behaviour, it is recommended to increase the amount of layers. The FML specimen that is 15% lighter than Aluminum alloy specimen shows identical result to Glare and Aluminum alloy specimens concerning dent depth (Fig. 13).

This research was a part of the project, “The research for the light-FML” under the contract with The Society of Japanese Aerospace Companies (SJAC).

References

- 1) R. Alderliesten, C. Rans, R. Benedictus, *Composites Science and Technology*, 68, 2983-2993 (2008)

- 2) Ad Vlot and J.W.Gunnink, Fibre Metal Laminates and introduction (2001), Kluwer Academic Publishers

2.6 Critical Distance for Fatigue Life Prediction in Aerospace Materials

Yoichi Yamashita, Yusuke Ueda and Hiroshi Kuroki

IHI Corporation

Foreign object damage (FOD) often causes small notches on leading edge of airfoil (Fig. 14). The previous paper [1,2] investigated the method for estimating the fatigue life of small-notched Ti-6Al-4V specimens using the theory of critical distance (CD). Critical distance stress is defined as the average stress within the critical distance from notch root using simple linear-FE results. However, the issues still remain that a general procedure to determine appropriate critical distances of aerospace materials and further verifications are needed. The materials used are Titanium alloy, Ti-6Al-4V, and Ni-base superalloy, In718.

A good correlation exists between the critical distance stress and fatigue life of small-notched specimens if the critical distance is calibrated by the two notched fatigue failure curves of different notch root radii (Fig. 14). In Ti-6Al-4V, the calibrated critical distances have an almost constant value from medium-low-cycle fatigue regime to high-cycle fatigue regime (Fig. 15(a)). The average critical distance corresponds to the depth of the crystallographic facets at the crack initiation sites (Fig. 16). In In718, the longer fatigue life gives the smaller critical distance (Fig. 15(b)). It can be seen that the critical distance is dependent on the yielding scale near notch tip, such as plastic zone size. Using these critical distances, the fatigue lives of various small notched specimens can be well predicted for a wide range of fatigue life (Fig. 16 for Ti-6Al-4V).

Other verification results are shown in the contact edge fatigue problem of the dovetail in aero-engine component. An analogy exists between a flat/rounded contact stress and a small notch stress fields [3]. The fretting fatigue may be predicted by using critical distance calibrated by the two fatigue failure curves of different notch root radii. Figure 17 shows the predictions compared to fretting fatigue test results [3] for flat and rounded contact pads on Ti-6Al-4V alloy specimens. There have been the possibilities that the predictions using critical distance give the reasonable fretting fatigue crack initiation lives.

References

- [1] Yamashita Y., Ueda Y., Kuroki H. and Shinozaki M. (2009), Proc of ICAF 2009.
- [2] Yamashita Y., Ueda Y., Kuroki H. and Shinozaki M. (2010), Eng Fract Mech, 77, 1439–1453.
- [3] Araujo JA. and Nowell D., (2002) Int J of Fatigue, 24, 763–775.

3. FATIGUE IN COMPOSITE MATERIALS AND COMPONENTS

3.1 Damage Tolerance Demonstration of Flange Joint for Aero Engine Composite Fan Case

Yusuke Ueda,¹ Hiroshi Kuroki,¹ Takeshi Murooka,¹ Agamu Tanaka,¹ Koji Miyazawa,¹ Ikuro Okumura,² Yu Shigenari,² Kazuki Oikawa,¹ and Hideo Morita¹

¹ IHI Corporation, Tokyo, Japan

² IHI AEROSPACE Co.,Ltd., Tokyo, Japan

Fan Case of aircraft turbo fan engines is located in the front end of a engine, and surrounds a periphery of fan blades. When a fan blade fails for some reasons, which is called fan blade out event, fan case needs to prevent high energy debris from penetrating through it. When a blade out event occurs, fan case is subjected to a very large load, which is called FBO load. FBO load is followed by repeated unbalance load due to wind milling while the aircraft returns to an airport after the event. Therefore fan case needs to endure not only the FBO load but also repeated unbalance load after the event. This is called “Fly home capability”. Also it is necessary to confirm that defects, such as delamination caused during manufacturing process, do not have the detrimental effects on the structure integrity requirements.

In this paper, the damage tolerance capability of a flange of a composite fan case was demonstrated. The test subcomponent specimens were cut from the ring with flange which was made in the same process with the actual composite fan case. The fan case was made of ± 45 degree laminates and 90 degree laminates, and their fiber was carbon, and their resin was thermoset. The subcomponent test specimens include artificial defects, which can be detected by non-destructive inspection.

Type A specimens have the artificial defects at its corner area, and Type B specimens have the artificial defect at its cylindrical area, as shown in Fig. 18. The condition of the cyclic load for the Flaw Tolerant Demo. and Fly Home Capability Demo. was determined by referring to the test sequence for strength, durability, and damage tolerance demonstration of CMH-17¹⁾.

First, the static tensile test was conducted with the test specimens which had two different sizes of defects, to confirm the effect of defect size. And it was confirmed that there was no significant difference in ultimate load capability due to the defects as shown in Fig. 19. And the behavior of the failure in the flange of the composite fan case was made clear.

Next, the test for Flaw Tolerant Demo. and Fly Home Capability Demo. were continuously conducted using the same specimen with the defect, whose size was detectable with sufficient confidence in consideration of the inspection method for the actual manufacturing process. During Flaw Tolerant Demo., no damage occurred and the stiffness of the specimens didn't change under normal fatigue cyclic load. Then, it was concluded that no detrimental damage occurred under normal fatigue cyclic load. During Fly Home Capability Demo., the stiffness of Type A specimen decreased by FBO Load, but the stiffness of Type B specimen didn't change. But the stiffness didn't change under unbalance fatigue cyclic load in both specimens as shown in Fig. 18. It was concluded that there was no growth of a damage. It was verified that the delaminations which was smaller than the allowable defect size on drawing didn't have the detrimental effect on the durability and Fly Home Capability as shown in Fig. 20.

Based on these test results, the capability of NDI at the manufacturing process was verified to be sufficient for the composite fan case.

This research was conducted as a part of the project, "Advanced Materials & Process Development for Next Generation Aircraft Engines" under the contract with Japanese Aero Engines Corporation (JAEC), funded by Ministry of Economy, Trade and Industry (METI) of Japan.

Reference

1) COMPOSITE MATERIAL HANDBOOK VOLUME.3. POLYMER MATRIX COMPOSITES MATERIALS USAGE, DESIGN, AND ANALYSIS, DEPARTMENT OF DEFENSE, UNITED STATES OF AMERICA

3.2 Multiaxial Damage Modeling of Bearing Failure in CFRP Bolted Joints Based on Fiber Compressive Failure Criterion

Takeaki Nadabe¹, Nobuo Takeda¹, and Masaaki Nishikawa²

¹ Department of Advanced Energy, Graduate School of Frontier Sciences, The University of Tokyo

² Department of Nanomechanics, Graduate School of Engineering, Tohoku University

The bearing strength for bolted joints of CFRP laminates is closely related to the compressive strength in the ply where the fiber direction is parallel to the bearing load, because the onset and growth of kinking damage is one of the most important factors in the bearing failure. The ply compressive strength in the fiber direction largely depends on the shear stresses and the lateral constraint through the micromechanics on fiber kinking. Therefore, it should be modeled to accurately predict the strength of bolted joints. This study proposes a numerical model for addressing the damage evolution in bolted joints of CFRP laminates based on the fiber compressive failure criterion under multiaxial stress states.

The fiber compressive failure criterion is developed based on the fiber microbuckling model with matrix non-linearity given by Sun and Jun¹⁾. First, the relationship between the remote stresses and the local stresses in matrix is considered in the composite with aligned fiber, and the effective stress in matrix is represented by the remote stresses (Fig. 21). Then, the critical microbuckling stress can be obtained based on the fiber microbuckling model. By incorporating this failure criterion in each finite element considering its stress state, the damage initiation and propagation in CFRP bolted joints are modeled.

The simulated damage area is compared with the experimental damage area obtained by a soft X-ray photography (Fig. 22). We demonstrate that the simulated agree with the experimental results (Fig. 23).

Reference

- 1) C. T. Sun and A. W. Jun, *Compos. Sci. Technol.*, **52**, 577(1994).

4. STRUCTURAL HEALTH MONITORING

4.1 Memorization and Detection of an Arrested Crack in a Foam-core Sandwich Structures Using Embedded Metal Wires and Fiber-optic Sensors

Shu Minakuchi*, Nobuo Takeda*, and Yasuo Hirose**

* The University of Tokyo

** Kawasaki Heavy Industries, Ltd. (KHI)

Foam-core sandwich structures are attracting considerable attention as a way to maximize the potential of carbon fiber reinforced plastic (CFRP). The integral construction consists of two thin CFRP facesheets and a lightweight foam core, which can considerably reduce the weight and the number of parts compared to conventional structures. However, crack propagation along the interface between the facesheet and the core is a critical issue. In this context, a crack arrester (Fig. 24) was recently developed to suppress interface crack propagation. The crack arrester is a semi-cylindrical stiff material inserted into the interface. The crack arrester decreases the energy release rate at the crack tip by suppressing local deformation around the crack. If the arrested crack can be instantaneously detected, the damage tolerance of foam-core sandwich structures can be dramatically improved. This study established an innovative crack detection technique using metal wires and fiber Bragg grating (FBG) sensors embedded at both edges of the arrester. The change in strain distribution in the arrester induced by arresting the interface crack was first memorized by the metal wire and the consequent residual strain distribution after unloading was then picked up by the FBG sensor as a damage signal (Fig. 25).

In this study, a Mode I type crack was evaluated using a double-cantilever beam (DCB) sandwich specimen. We began by simulating sensor responses to evaluate the feasibility of the proposed technique. Elasto-plastic finite element analysis of the specimen was conducted under loading/unloading condition and residual strain in the sensor obtained after unloading was then utilized to estimate changes in the reflection spectrum from the FBGs. When the crack arrester suppressed the crack propagation, shear deformation of the arrester was induced at the crack-side edge, and, consequently, the metal wire embedded at the edge plastically deformed. After unloading, the plastic strain in the metal wire induced residual strain in the FBG sensor, changing the reflection spectrum from the sensor due to a birefringence effect. However, since spectra, obtained from the sensor at

the opposite side of the crack, did not change, it was expected that the crack propagation direction can be determined by utilizing reflection spectra from the two FBG sensors embedded at both side edges of the crack arrester (Fig. 25).

Finally, a verification test was conducted (Fig. 26). First a new technique was developed to embed the metal wires and the FBG sensors at desired position, and the facesheets and the arrester were then co-cured with the foam core in an autoclave. At the test, once the crack propagated, the test machine was stopped, and the reflection spectra from the two FBG sensors were recorded. The test was then resumed, and this procedure was repeated until the crack reached the arrester edge. The measured spectral responses agreed well with the simulation results, confirming that the spectral change of the FBGs can clearly indicate the crack propagation direction immediately after arresting the crack. Thus the proposed technique enables an effective application of the crack arrester and significantly improves the reliability of foam-core sandwich structures.

SM and NT acknowledge the support from the Ministry of Education, Culture, Sports, Science and Technology of Japan under a Grant-in-Aid for Scientific Research (S) (No. 18106014).

4.2 Damage Detection of CFRP Bolted Joints Using Embedded Optical Fibers with BOCDA System

Shu Minakuchi, Takeaki Nadabe, Nobuo Takeda, Hajime Kishi, and Kazuo Hotate
The University of Tokyo

The authors propose fiber-optic-based damage monitoring of carbon fiber reinforced plastic (CFRP) bolted joints. Optical fibers were embedded along bolt holes and strain change along the optical fiber induced by internal damage was measured by a Brillouin Optical Correlation Domain Analysis (BOCDA), which is a high spatial resolution distributed strain sensing system. This study began by investigating damage modes of CFRP bolted joints after bearing failure. Effective embedding positions of optical fibers were then proposed and their feasibility was evaluated by finite element analysis simulating the damage propagation in the bolted joint and consequent strain change. Finally, verification tests were conducted using specimens with embedded optical fibers at various positions (Fig. 27). It was clearly shown that damage could be detected using residual strain due

to fiber-microbuckling (kinking) damage or permanent deformation of neighboring plies (Fig. 28). Furthermore, damage size and direction could be estimated from the change in the strain distribution. The system developed is quite useful for a first inspection of large-scale composite structures in aerospace applications (Fig. 29).

SM and NT acknowledge the support from the Ministry of Education, Culture, Sports, Science and Technology of Japan under a Grant-in-Aid for Scientific Research (S) (No. 18106014).

4.3 Full-Field Damage Detection System for Scarf Repaired Composite Structures Using Pulse-Laser Generated Lamb Waves

Yusaku Ito, Ichiya Takahashi and Nobuo Takeda

The University of Tokyo

A scanned pulse-laser generated wave-visualized technique was applied to impact damage detection in scarf-repaired composite (Fig. 30). This technique can make it possible to visualize the ultrasonic wave propagation in scarf-repaired composite. When propagating waves scatter or reflect at the damage area, we can detect damages by observing the visualized wave propagation (Fig. 31). Scarf-repaired composites with an artificial defect simulating impact damage were inspected by using this wave-visualization technique (Fig. 32). Simulation and inspection of specimens with coating were also done for evaluating influence of coating on the damage detection using this wave-visualization technique (Fig. 33). As a result, scattering and reflection of visualized ultrasonic waves were observed around the damage area in scarf-repaired composites with or without coating. This result indicates the wave-visualized technique is useful in inspection of scarf-repaired composites.

NT acknowledges the support from the Ministry of Education, Culture, Sports, Science and Technology of Japan under a Grant-in-Aid for Scientific Research (S) (No. 18106014).

5. LIFE EVALUATION ANALYSIS

5.1 A Structural Defect Expansion Model Based on Physical Correlation

Seiichi Ito, Sunao Sugimoto and Takao Okada
Aviation Program Group, Japan Aerospace Exploration Agency (JAXA)

The spatial correlation and time dependence parameters of aging structural defects are evaluated on the basis of a percolation model. Probabilistic model parameters are obtained by the Markov chain Monte Carlo (MCMC) method using a Bayesian theory framework. The generality of this model is verified on the basis of numerical simulation using the free software "R".

The probability of defect initiation and its expansion on a structural surface is modeled based on two-dimensional percolation. In addition, a multilayer laminated structure of overlapping two-dimensional models is assumed to describe the space and time correlations of a three-dimensional structural defect. This model can also be applied to an uncertainty evaluation of the expansion of an aging defect by considering the laminations to represent the sample thickness.

A structural part is divided into homogeneous unit elements at the beginning of the modeling. Within these elements, a Poisson process is assumed to govern the probability of a defect occurring in a unit of time. A Poisson model is also used for the correlation of defect expansion between elements. In addition, a simple limiting condition is assumed for expansion in the direction of defect depth. This method can be used in the evaluation of the expansion of corrosion defects. Because the distribution of the defect area and the corrosion depth directly influence structural strength and rigidity, it is important to comprehend the spatial pattern of the defect in order to evaluate structural integrity (Fig. 34).

In the calculated example, the initial parameters of the probabilistic model are set, and a virtual structural defect expansion model is created by the numerical simulation. The unknown parameters of defect initiation and expansion are assigned based on a virtual defect using a Bayesian estimation method, and the validity of this model is verified. Because the posterior distribution of the unknown parameters is complex, the metropolis method of MCMC is applied here (Fig. 35).

A concrete numerical calculation example is shown in the following figures (Figs. 36-38). Applying this model to a real structural defect requires calibration for the structural defect by means of a parametric study using MCMC. The uncertainty in the progression of an aging structural defect can be appropriately evaluated by applying this model in such a way that the correlation of space and

time is determined by the three-dimensional evaluation model. The excellent free and open-source software "R" is used for the above calculation.

Since the aging structural defect contains a lot of uncertainty factors, the strict evaluation of the defect is generally difficult. To overcome this, the calculation statistics was introduced into the defect evaluation process. Using the probabilistic percolation model, the proposed method can be applied to the expansion evaluation for aging structural defect and the laminated material defect in the real structures.

6. FULL-SCALE TESTING

6.1 XP-1/XC-2 Full Scale Strength Test

T. Okazaki

Air Systems Research Center, Technical Research and Development Institute (TRDI), Ministry of Defense, Japan

TRDI has been conducting simultaneous development of the next-generation maritime patrol aircraft (XP-1) and the next-generation cargo transport (XC-2). XP-1 is the successor of P-3C aircraft currently operated by Japan Maritime Self-Defense Force, and XC-2 is the successor of C-1 by Japan Air Self-Defense Force. The contractor of the development program is Kawasaki Heavy Industries Ltd.

XP-1 has following characteristics of the airframe structure.

- Main wing: Low-wing arrangement fitted with the main landing gear which is stored into the fuselage
- Tail wing: Conventional form
- The fuselage is designed to ensure the space for equipment and crew's working area.

XC-2 has following characteristics of the airframe structure.

- Main wing: High-wing arrangement for installing freights
- Tail wing: T-tail form
- The fuselage has the large-scale freight door in the after section.
- Main landing gear storage: Bulge form to ensure the freight room

This simultaneous development of XP-1 and XC-2 contributes to the life-cycle cost reduction by sharing the design technique, equipment, and airframe structure (part of the cockpit, outboard part of the main wing and the horizontal tail).

The FSST (Full Scale Static Test) airframes of XP-1 and XC-2 were delivered to evaluate the static strength of the airframe structure in 2006, and the FSFT (Full Scale Fatigue Test) airframe of XP-1 was delivered in 2007, and the FSFT airframe of XC-2 was delivered in 2010. Each airframe is neither painted nor equipped with any instruments because of unnecessary for the evaluation.

The FSST consists of the limit load tests and the ultimate load (1.5times the limit load) tests. It is to demonstrate static strength of airframe by simulating a variety of design loads, such as maneuver, gust, and landing loads, using lots of actuators controlled synchronously.

The FSFT consists of the durability test and the damage tolerant test, both of which are conducted for two life-times of spectrum loading for validation.

The maiden flights of XP-1 and XC-2 were conducted successfully in 2007 and 2010 respectively (Fig. 39).

The limit load tests and the ultimate load are executed one by one in FSST of XP-1 and XC-2 (Fig. 40). Moreover, the durability test is being executed in FSFT of XP-1 and XC-2.

6.2 Durability and Damage Tolerance Evaluation of VaRTM Composite Wing Structure

Yuichiro Aoki, Yoshiyasu Hirano, Sunao Sugimoto, Yutaka Iwahori, Yosuke Nagao, and Takeshi Ohnuki

Aviation Program Group, Japan Aerospace Exploration Agency (JAXA)

Vacuum-assisted resin transfer molding (VaRTM) is a promising cost-effective fabrication method for manufacture of aircraft components. It features lower tooling costs, ease of scalability and applicability of large complex geometry. JAXA has demonstrated the high quality and performance of VaRTM composites through 6m VaRTM wing development research project since 2004¹⁾. In this study, durability and damage tolerance of sub-component and full-scale wing box structure fabricated by VaRTM are evaluated. The first phase is fatigue tests to verify durability of the structure without any artificial damages. Fatigue spectrum

with load enhancement factor was applied to the test articles for 1 DSO (Design Service Objective) that is equal to 40,000 flights. The second phase is evaluation of visible and barely visible impact damages growth to verify damage tolerance of the structures during 1 DSO and to estimate optimal inspection intervals and evaluate the residual strength of structure. Impact damages are given to the skin stiffened by co-cured stringer and typical skin part by drop-weight to create the delamination. Applied strain level for sub-components are intentionally higher than original one in order to evaluate the structural performance in more critical condition. The Mini-TWIST²⁾ fatigue spectrum is used for both tests. Non-destructive inspection is carried out by three-dimensional ultrasonic scanning system with multiple-array sensors to evaluate delamination growth. Finally, static load is applied up to 150% design limit load to verify the residual strength after 2 DSO fatigue tests. In sub-component test, stringer run-out shows local out-of-plane deformation and that causes disbonding of stringer tip. The disbonding area gradually increases during 1 DSO fatigue test (Fig. 41). However, the present structure did not show any degradation of structural performance. The damage tolerance tests verify that impact-induced delaminations have not grown throughout the 1 DSO. In the final ultimate load test, the load bearing-capabilities of the present VaRTM wing structure were verified and the structure could survive for 4 seconds without any detrimental deformation and damage growth (Fig. 42).

References

1. Review of Aeronautical Fatigue Investigations in Japan during the period July 2007 to May 2009, Edited by H. Terada and N. Takeda, Presented at 31st Conference of the International Committee on Aeronautical Fatigue (ICAF), Rotterdam, The Netherlands, 25-26 May 2009, p. 21-23.
2. H. Lowak J. B. de Jonge, J. Franz and D. Schütz, MINITWIST – A shortened version of TWIST, NLR MP 79018 U, 1979.

7 AIRCRAFT ACCIDENT INVESTIGATION

7.1 Aircraft Accident Investigation and Aircraft Serious Incident Investigation

Ikuo Takagi

Japan Transport Safety Board (JTSB)

(1) Total number of registered aircraft in Japan

As of September 30, 2010, the number of registered civil aircraft in Japan was 2,722, consisting of 1,262 airplanes (of which 526 airplanes with jet engines), 789 helicopters, 670 gliders inclusive of motor gliders and an airship.

(2) Statistics related to the accident and serious incidents investigation

The number of accidents and serious incidents which JTSA investigated in the past two years are shown in Tables 4 and 5. Of the total of 54 occurrences, large airplanes accidents and serious incidents were 17, small airplanes were 12, and rotorcrafts were 14. Gliders, ULP (ultra light plane)s and others were remaining 11 occurrences.

(3) Fatigue failure related serious incident

1) Summary of the serious incident and probable cause

A Boeing 767-300 aircraft took off from an airport at 16:45 (Japan Standard Time, UTC+9h) on December 1, 2005 (Friday). Immediately after takeoff, vibration started on the right engine, and at about 16:48 the fire warning on the right engine was activated. The flight crew shut down the right engine and returned to the airport at 17:04 for a successful single engine landing.

It is considered highly probable that this serious incident was caused as follows: When the aircraft became airborne, one of the 2nd stage high-pressure turbine (HPT) blades of the right engine was fractured which had had considerable fatigue crack, leading other blades to be fractured which caused vibration to the right engine from unbalanced rotation, and the vibration further caused fracture of the fuel supply tube #6 inside the shroud can, moreover, the retaining ring at the end of the shroud can was dislodged by the pressure of fuel injected in the shroud can as well as by the engine vibration causing the fuel to leak, then the fuel was ignited when it contacted the hot section, and resulted in a flame in the engine designated fire zone.

2) Fracture of the HPT blades

The three separated HPT 2nd stage blades were #58, #57, and #56, in the order from the least remaining portion. Because Blade #58 exhibited characteristics consistent with low-cycle fatigue, it is considered probable that Blade #58 was the first separated one.

This serious incident was the first case in which the HPT 2nd stage blade made of DSR142 material was fractured. The fractured surface was perpendicular to the grain boundary of DSR142.

(See Figs. 43 and 44)

3) Factors contributed to the fracture of the HPT blade

Although the exact cause of the fatigue crack found in the turbine blade could not be determined precisely, it is considered possible that the following factors were combined and contributed:

① Because the TA (turnaround) radius of the cooling air passage inside the blades was smaller, the stress was prone to concentrate on that area and thereby it became prone to cause cracks, and later, the cracks progressed due to low-cycle fatigue. (See Fig. 45)

② Because sulfur was detected from the rupture surface, the blade was in the condition that crack came by hot corrosion. (See Fig. 46)

③ Thinner LE (leading edge) passage wall of the shank created the high stresses on the entire blades. (See Fig. 47)

ACKNOWLEDGEMENTS

The editors appreciated the members of the ICAF national committee of Japan Society for Aeronautical and Space Sciences, for their contribution in preparation of this national review and continuing discussion in the committee.

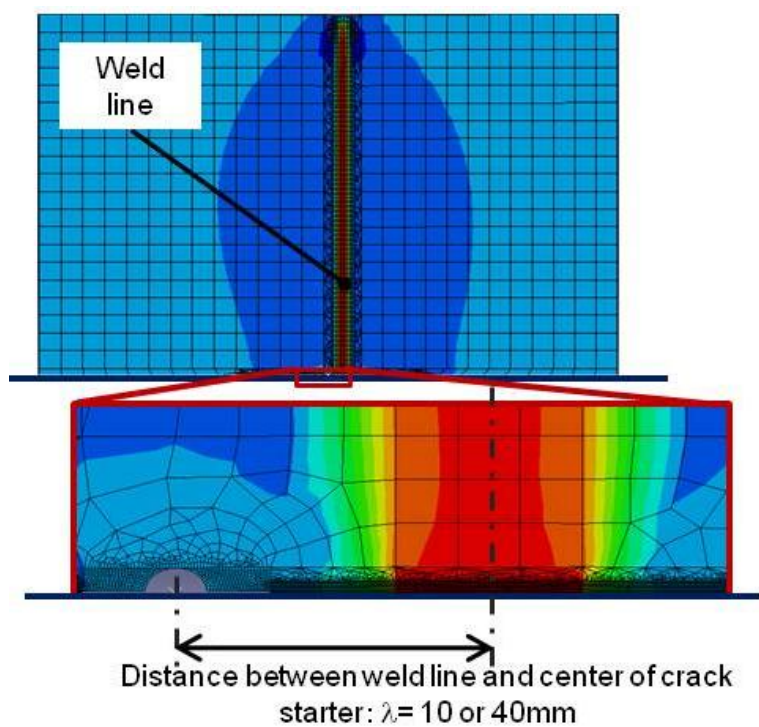


Fig.1 FEM model for FSW plate

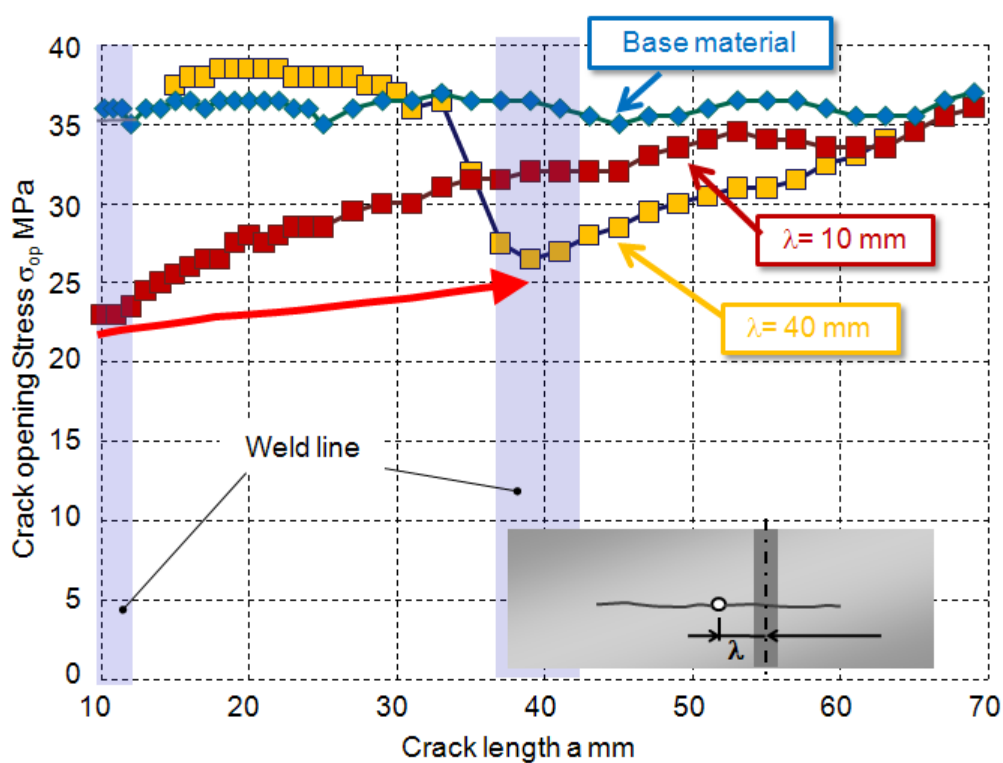


Fig.2 Crack opening stress distribution obtained by elasto-plastic FEM

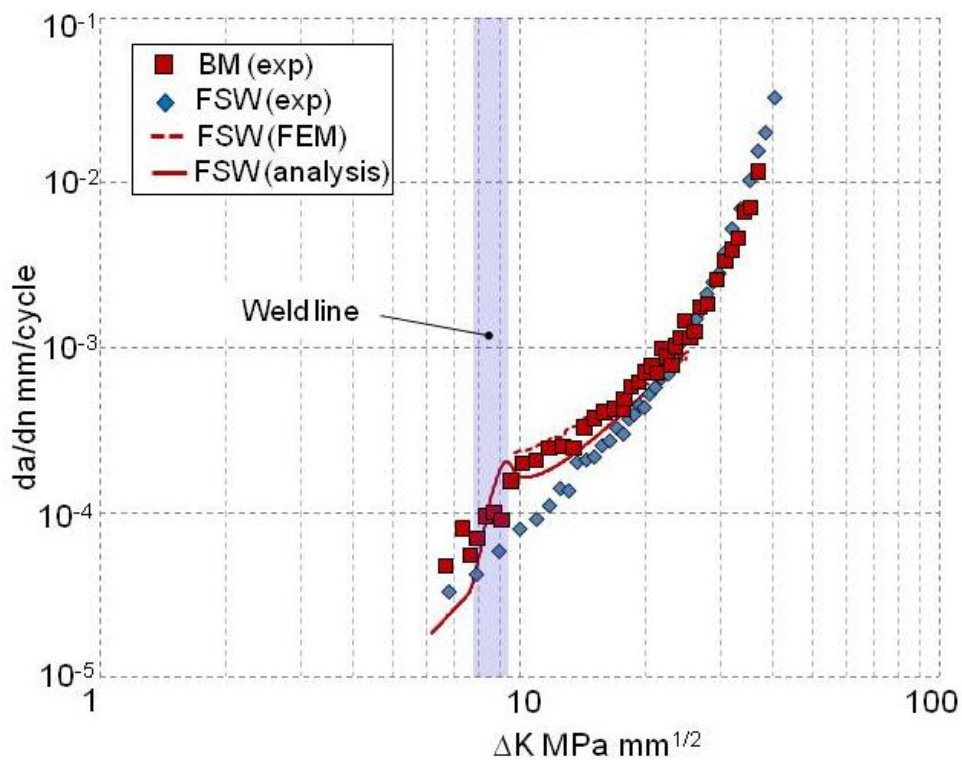


Fig.3 Comparison of fatigue crack growth rate

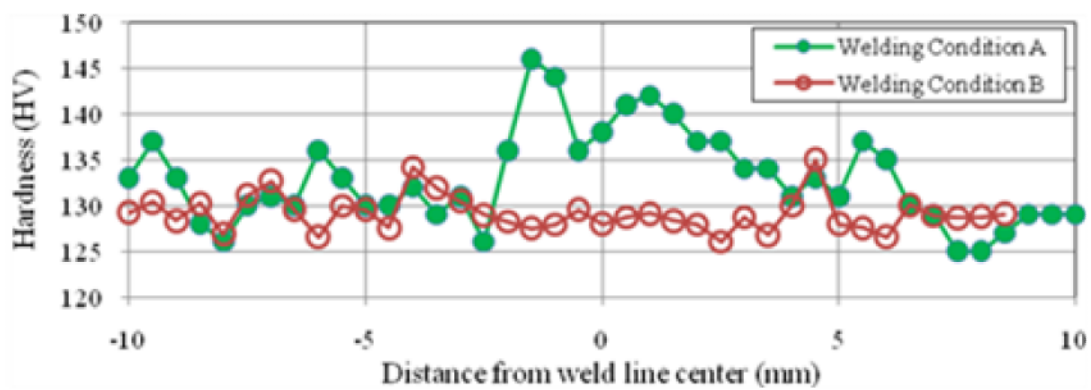


Fig. 4 Hardness profile perpendicular to the welding section

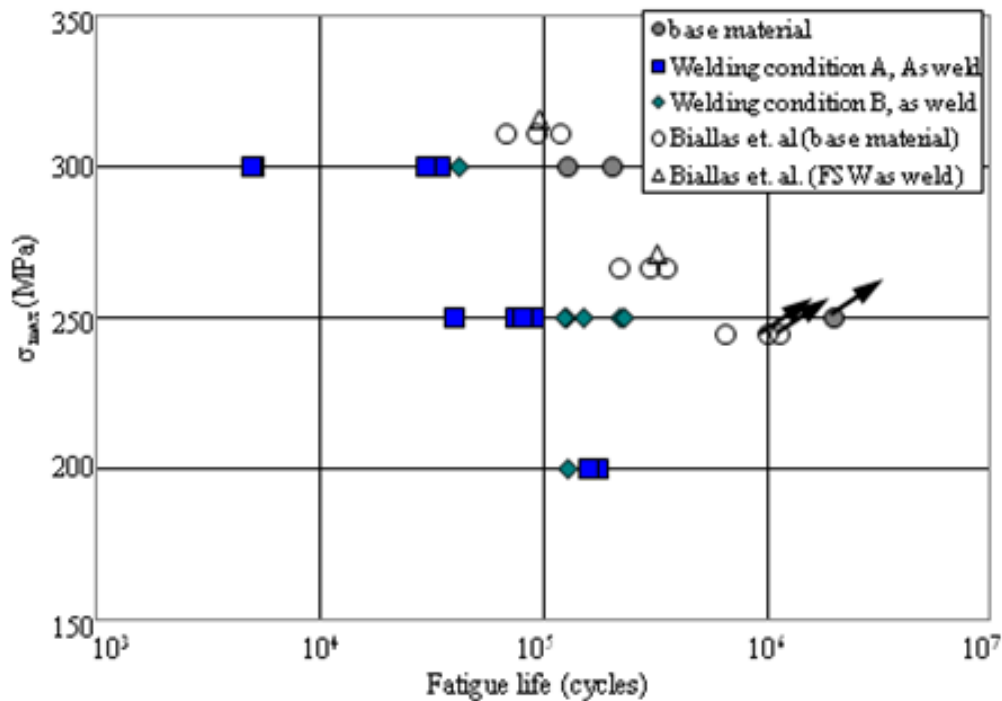


Fig. 5 Fatigue life for FSW specimen

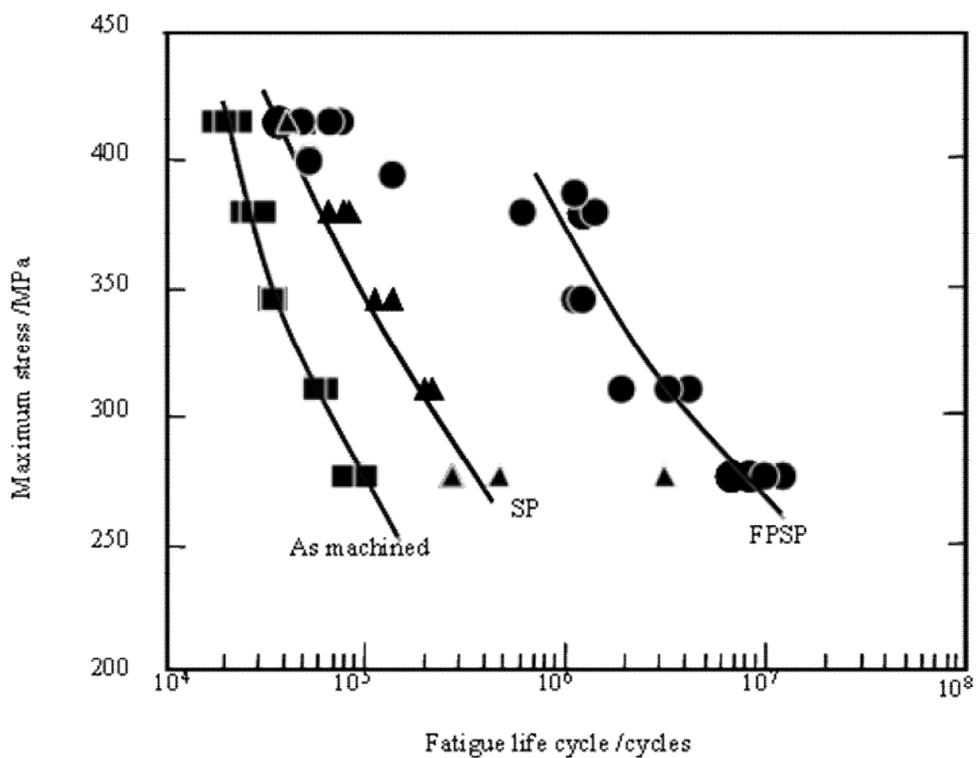


Fig. 6 Fatigue life cycles of 7050-T7451 round coupon

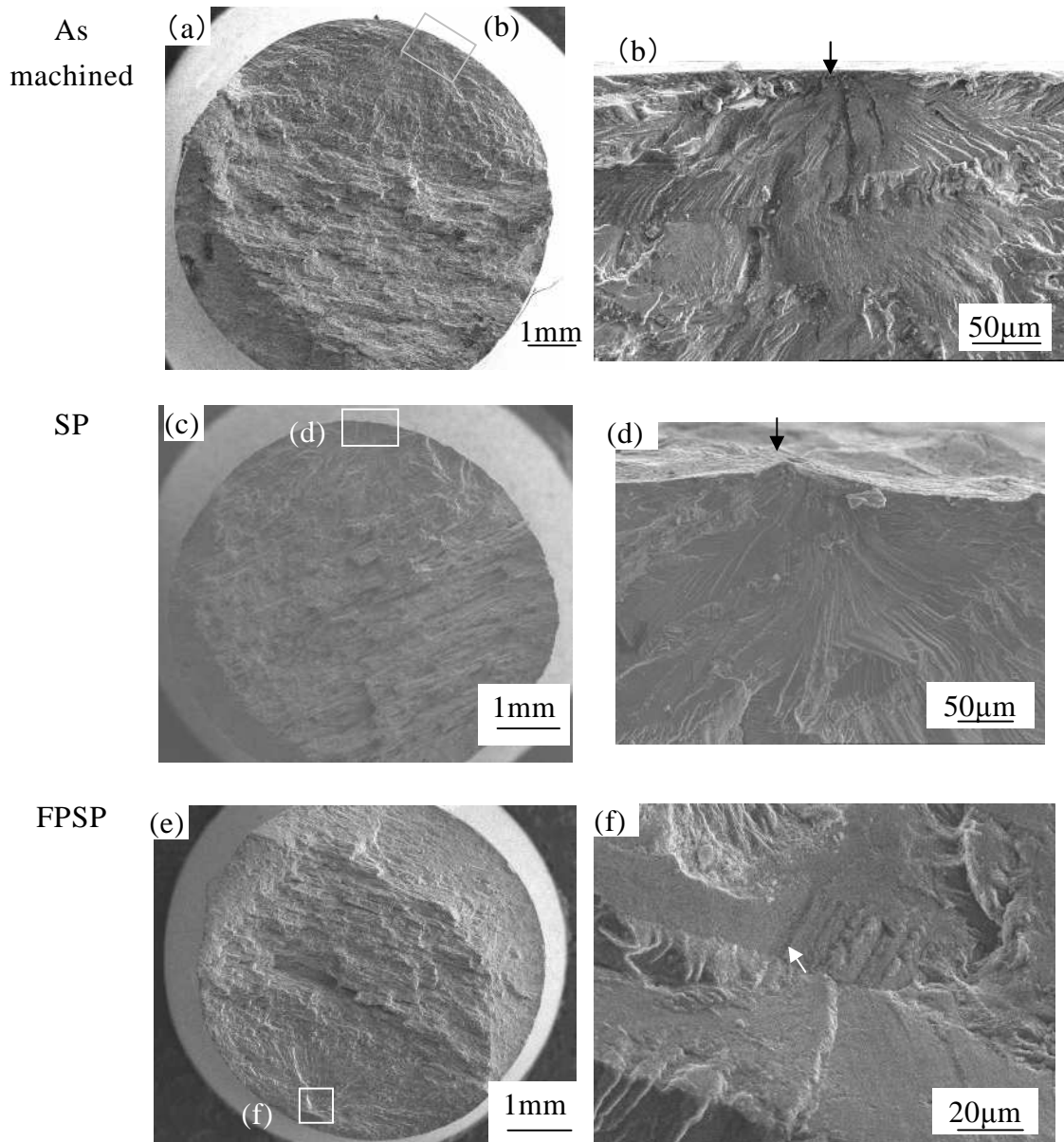


Fig. 7 SEM images of fatigue fractured surfaces

As machined specimen in (a) is magnified in (b). Shot peened specimen in (c) is magnified in (d) and FPSP specimen in (e) is magnified in (f). Arrows in (b) and (d) indicate the crack initiation site on the surface, while an arrow in (f) indicates subsurface crack initiation site. Maximum stress of fatigue testing is 344MPa.

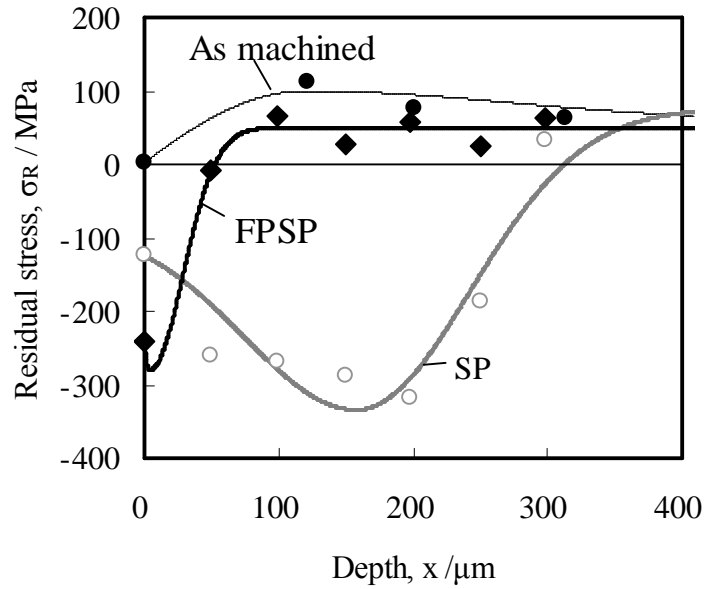


Fig. 8 X-ray residual stress measurement results. Each symbol is the experimental result and lines are approximated results derived by the least square method.

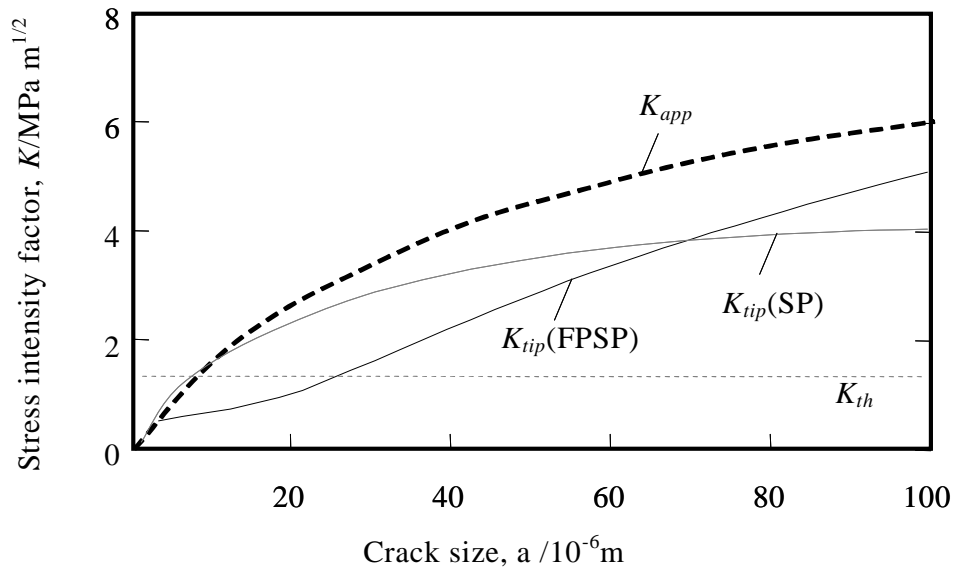


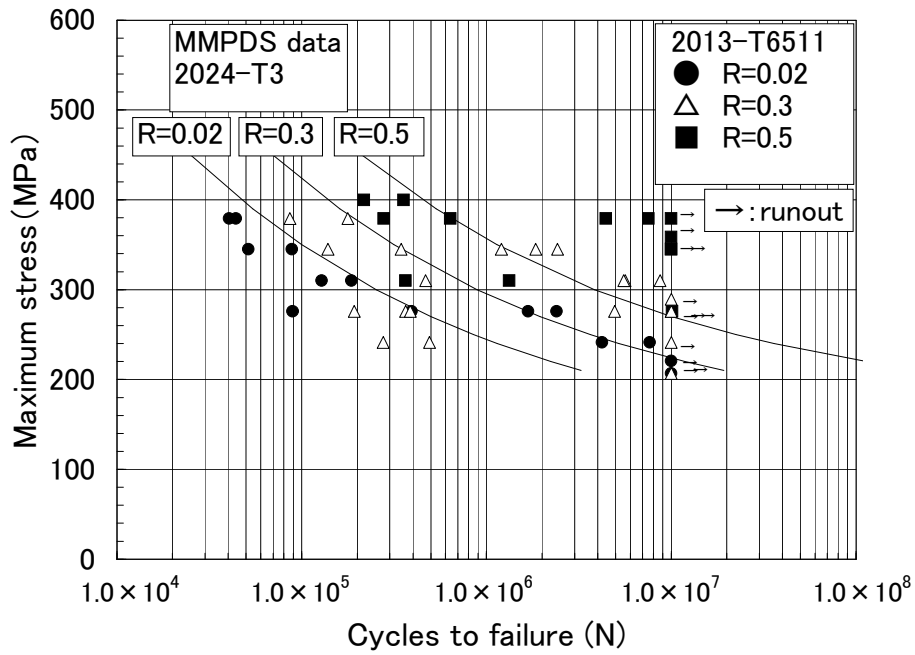
Fig. 9 Calculated stress intensity factors at the crack tip of SP and FPSP under the residual stress, K_{tip} and applied stress, K_{app} in comparison with the stress intensity factor threshold, K_{th} .

Table 1 Chemical Composition of Alloys (mass%)

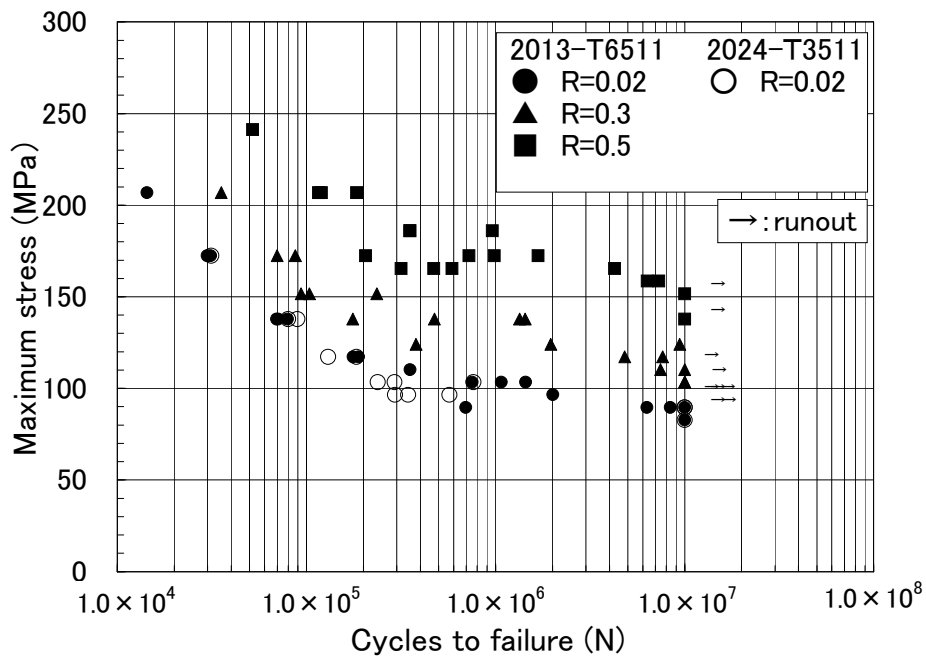
| Alloy | Si | Fe | Cu | Mn | Mg | Cr | Al |
|-------|---------|------|---------|----------|---------|-----------|------|
| 2013 | 0.6-1.0 | 0.40 | 1.5-2.0 | - | 0.8-1.2 | 0.04-0.35 | Rem. |
| 6013 | 0.6-1.0 | 0.50 | 0.6-1.1 | 0.20-0.8 | 0.8-1.2 | 0.10 | Rem. |
| 2024 | 0.50 | 0.50 | 3.8-4.9 | 0.30-0.9 | 1.2-1.8 | 0.10 | Rem. |

Table 2 Static Strength Properties

| | Tension | | Compre- ssion | Shear | Bearing (e/D=2.0) | | Bearing (e/D=1.5) | |
|---------------------------------|---------|-----|------------------|-------|----------------------|------|----------------------|------|
| | Fty | Ftu | Fcy | Fsu | Fbry | Fbru | Fbry | Fbru |
| Average (MPa) | 390 | 411 | 389 | 293 | 711 | 950 | 607 | 745 |
| A value (MPa) | 365 | 400 | 365 | 283 | 662 | 910 | 565 | 717 |
| 2024-T3511 A value (MPa) | 290 | 393 | 234 | 200 | 490 | 745 | 421 | 579 |
| 2013(A value) /2024(A value) | 1.3 | 1.0 | 1.6 | 1.4 | 1.2~1.4 | | | |



(a) $K_t=1.0$



(b) $K_t=3.0$

Fig. 10 Maximum stress versus fatigue life

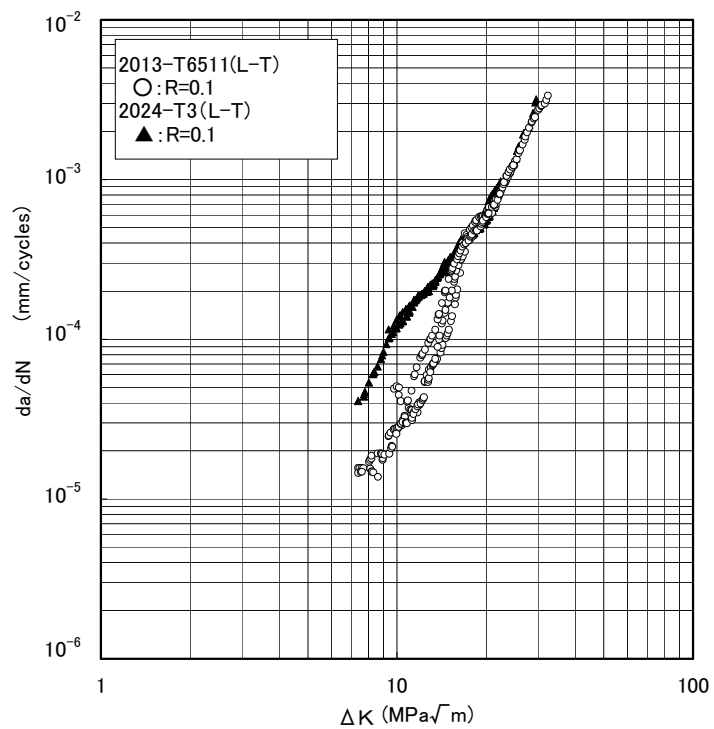
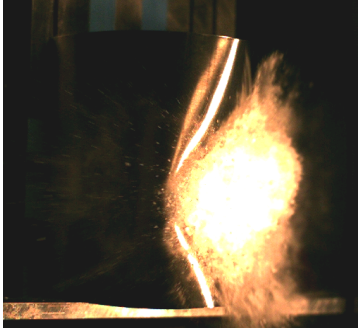
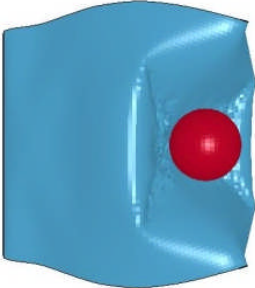
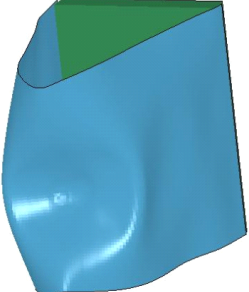
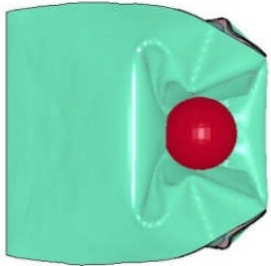


Fig. 11 Fatigue crack growth rate versus stress intensity factor

Table 3 Experimental and the numerical analysis results of the hail impact test

| Material | Mg-Li FML | Al |
|--|---|--|
| Experimental result (max. deformation) |  |  |
| Numerical result (without the primary delamination) |  <p data-bbox="539 1093 911 1216"><u>Without induced delamination</u> Differ from the figure of experimental result</p> |  <p data-bbox="995 1093 1315 1216">Almost agreement with the figure of experimental result</p> |
| Numerical result (with the primary delamination) |  <p data-bbox="555 1574 890 1742"><u>With induced delamination</u> Almost agreement with the figure of experimental result</p> | - |

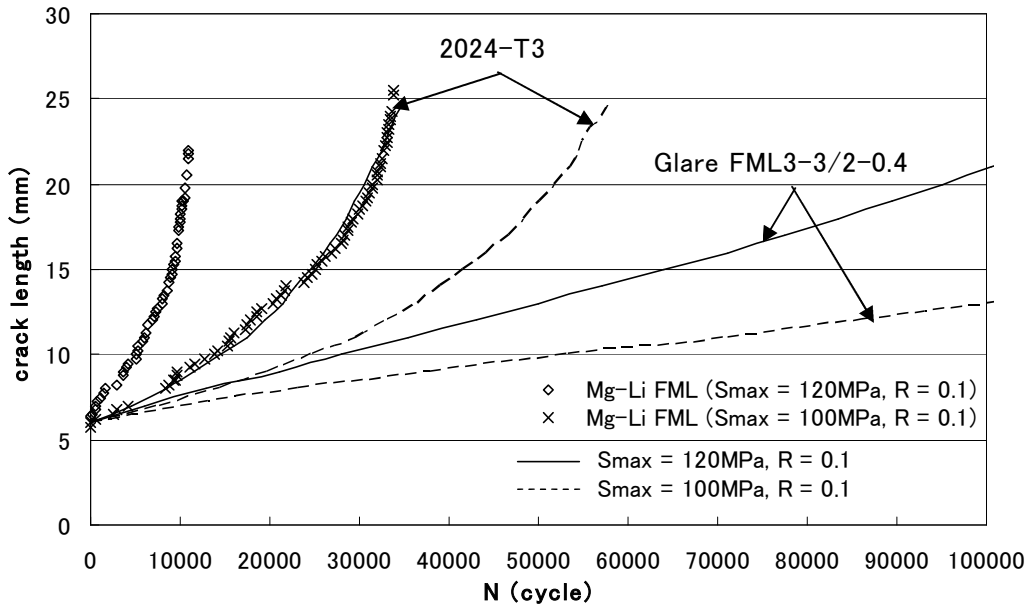


Fig. 12 Fatigue crack growth curves and the predicted fatigue crack growth curves of Alminum and Glare¹⁾

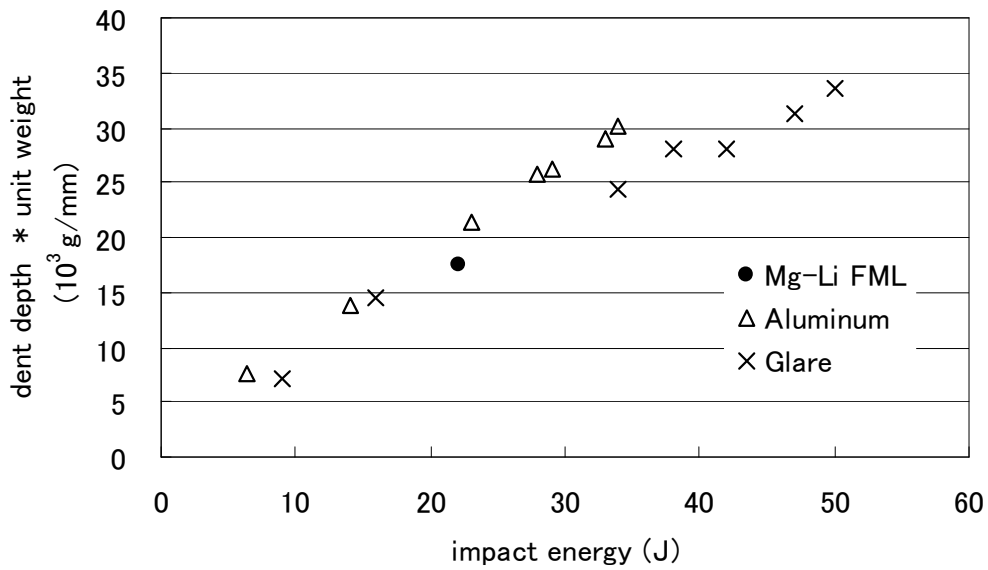


Fig. 13 Dent depth times unit weight versus impact energy with the result of Alminum and Glare²⁾

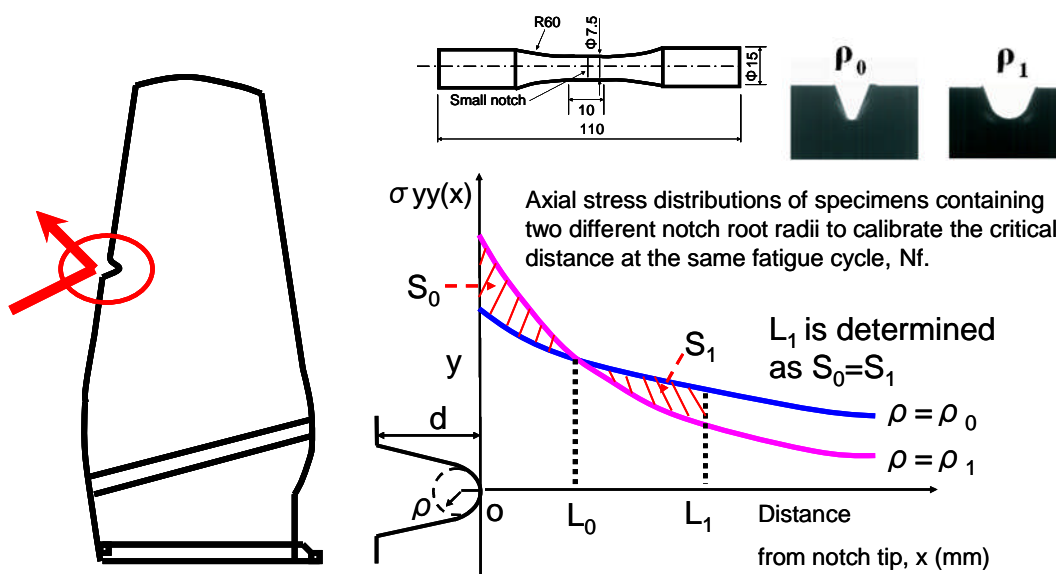


Fig. 14 Schematic of small notched fan blade and calibration of critical distance

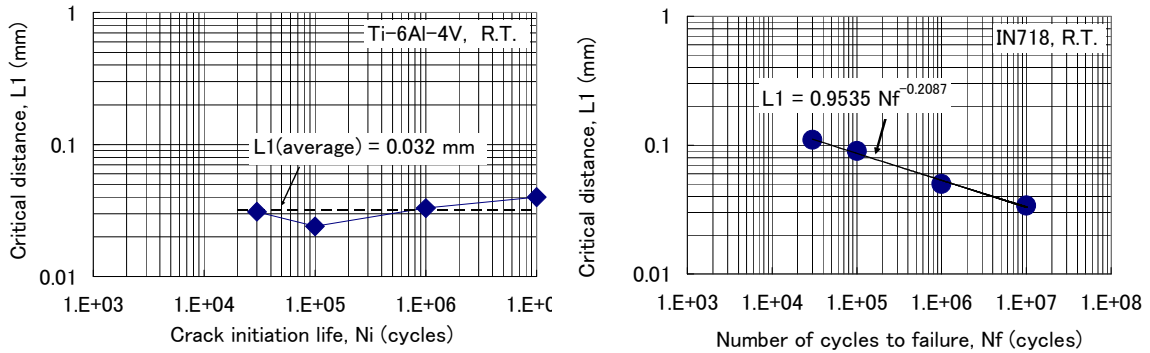


Fig. 15 Critical distances determined for aerospace materials

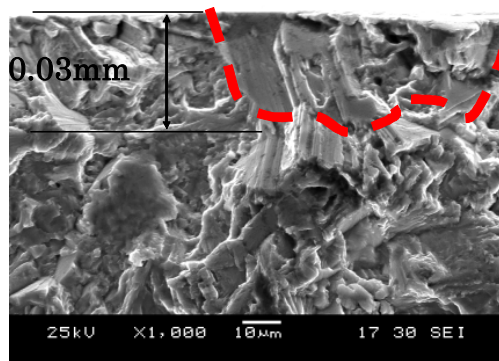
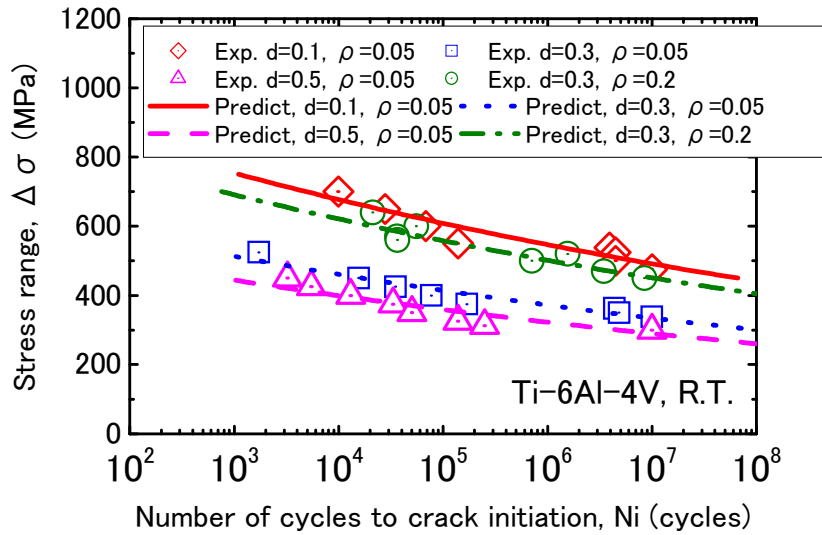


Fig. 16 Predictions using the critical distance for small notched Ti-6Al-4V specimens

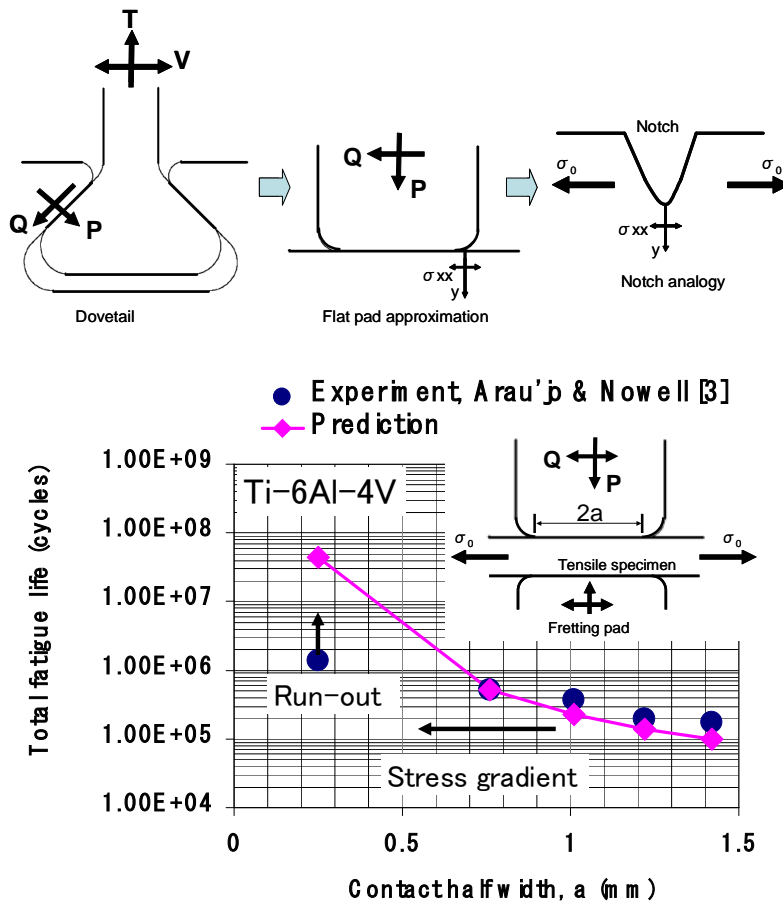


Fig . 17 Predictions using critical distance compared to fretting fatigue test results for contact pads on Ti-6Al-4V alloy specimens

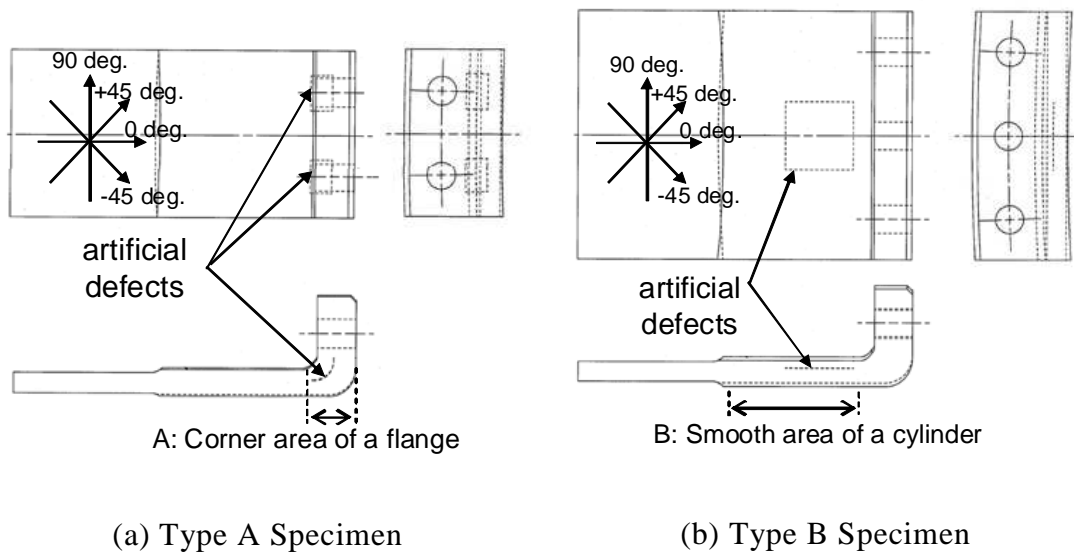


Fig. 18 Schematic Views of Specimens

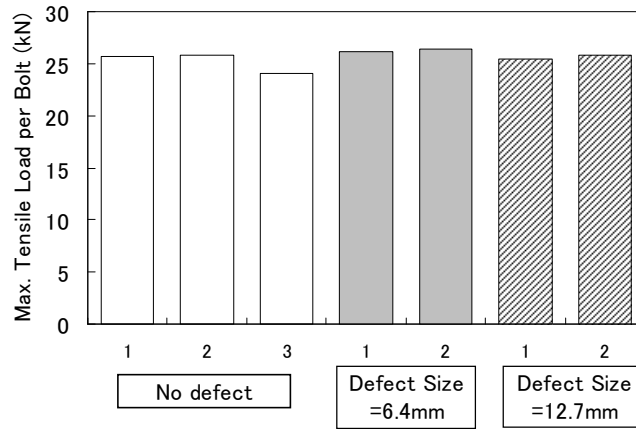
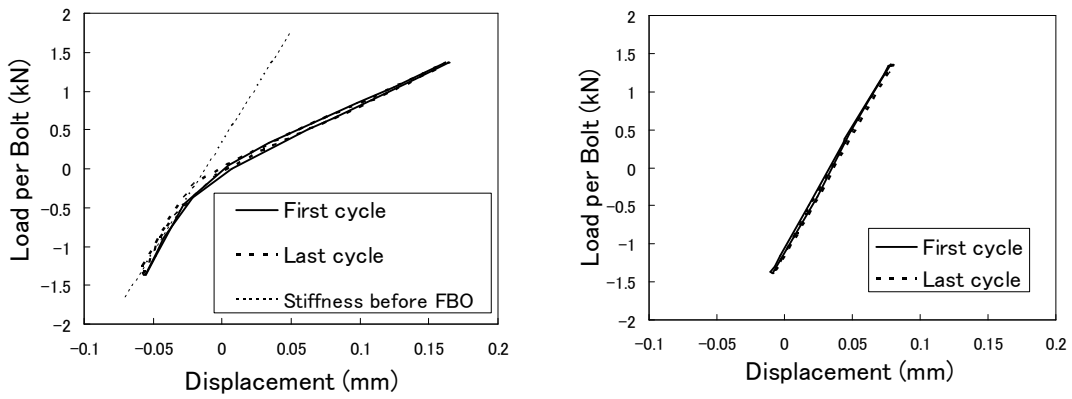


Fig. 19 Ultimate Load Capability of Type A Specimen



(a) Type A Specimen

(b) Type B Specimen

Fig. 20 Displacement-Load Curve under Unbalance Fatigue Load Cycle for Fly Home Capability Demo.

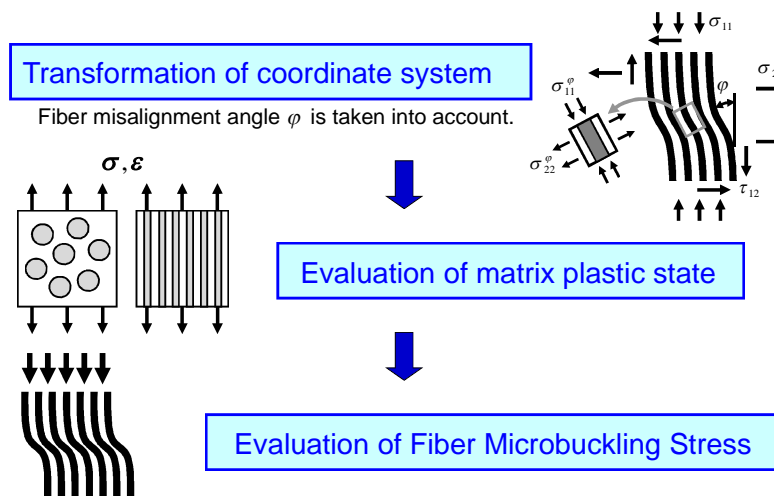


Fig. 21 Fiber microbuckling under multiaxial stress states

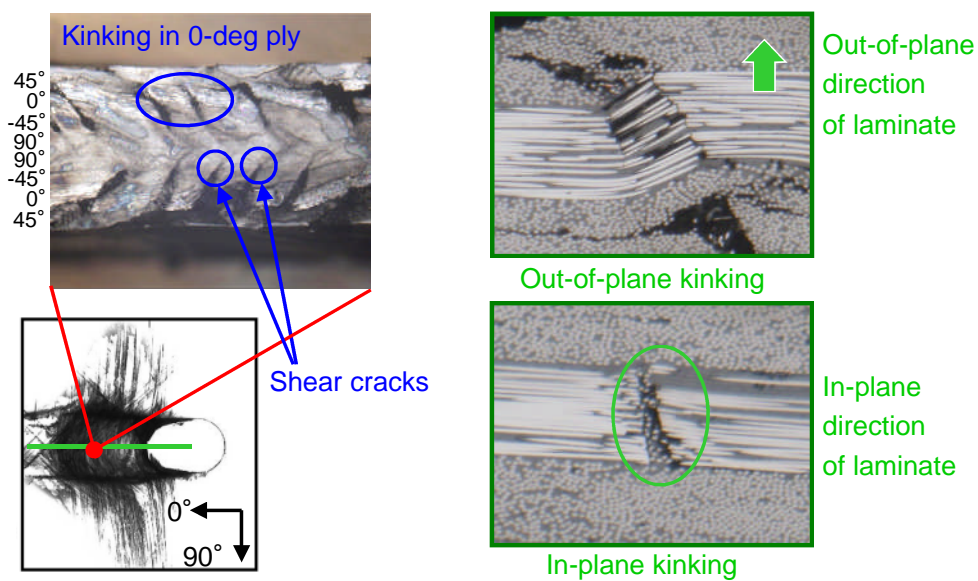
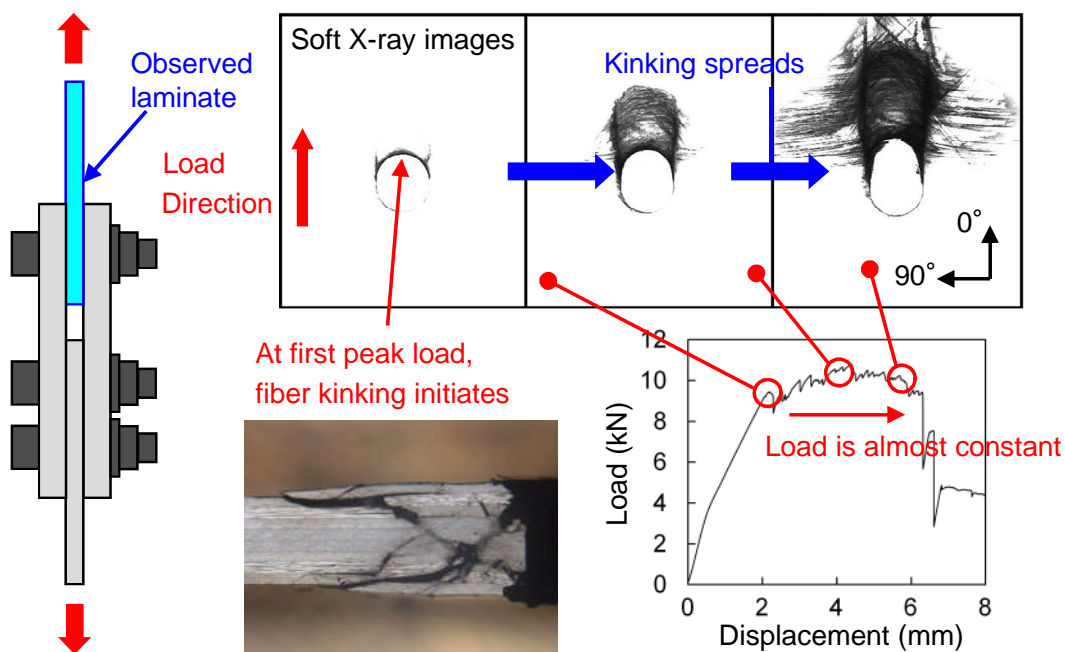


Fig. 22 Observation of bearing failure in CFRP bolted joints

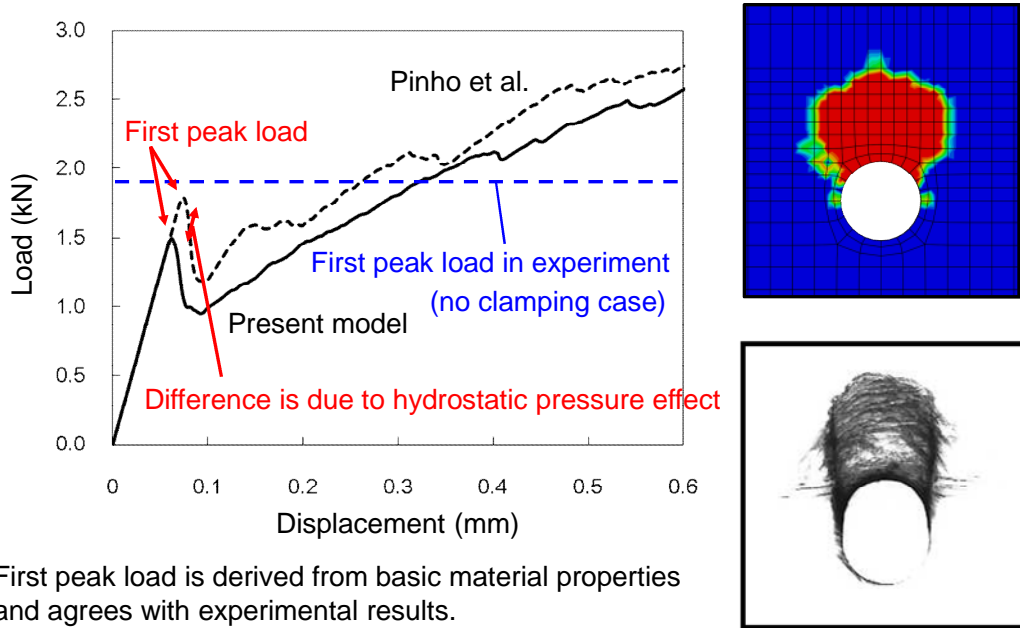


Fig. 23 Comparison between simulation and experiments.

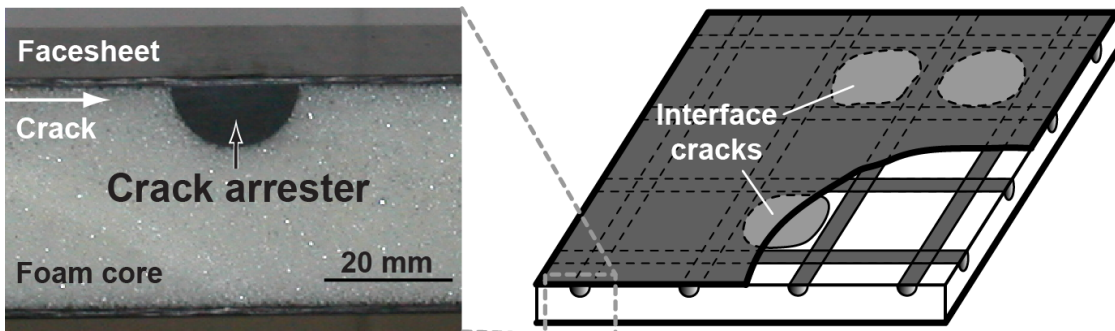


Fig. 24 Crack arrester in foam-core CFRP facesheet sandwich structure

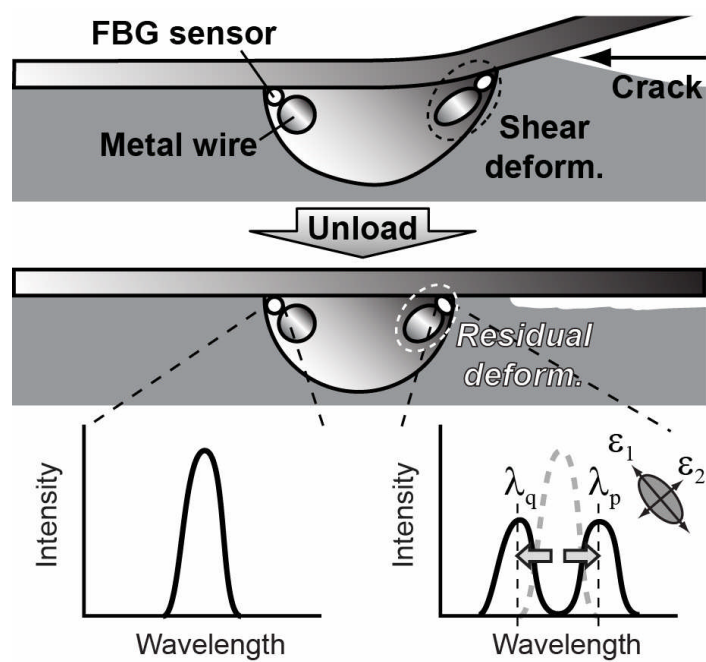


Fig. 25 Schematic of crack detection technique

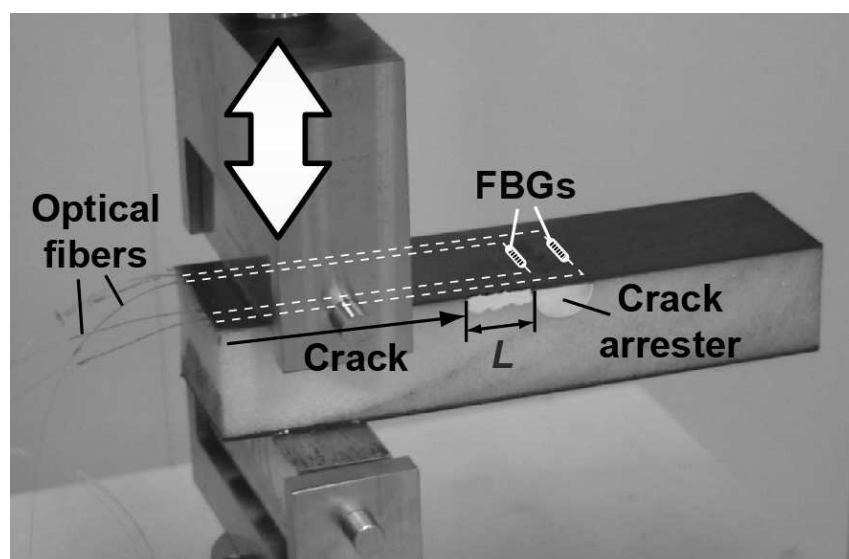
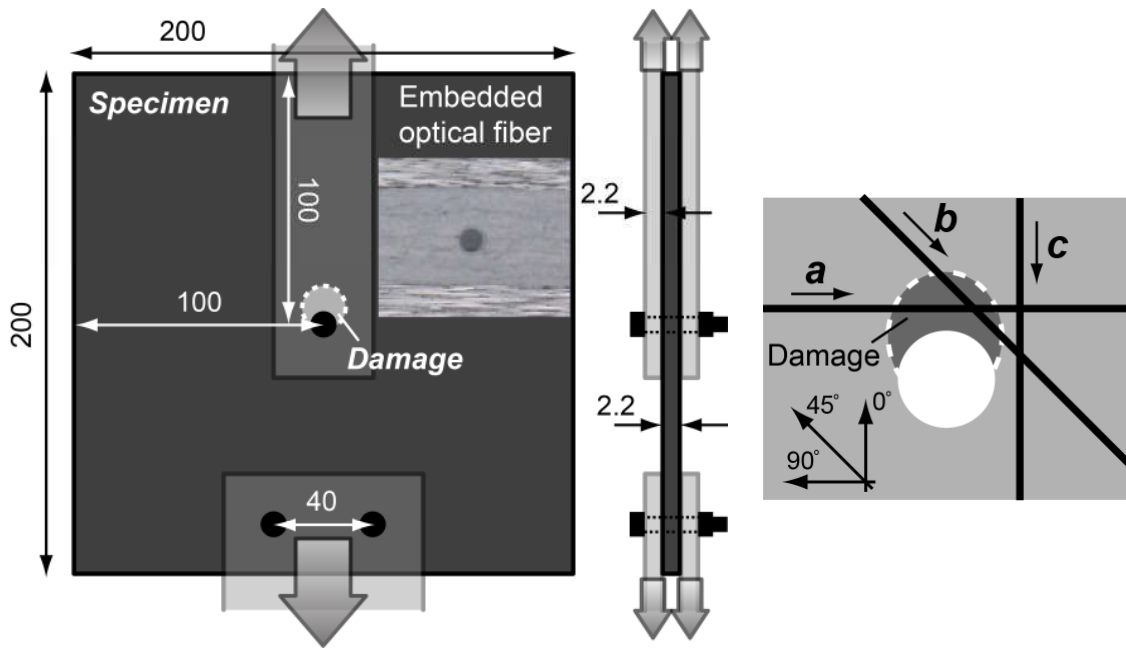
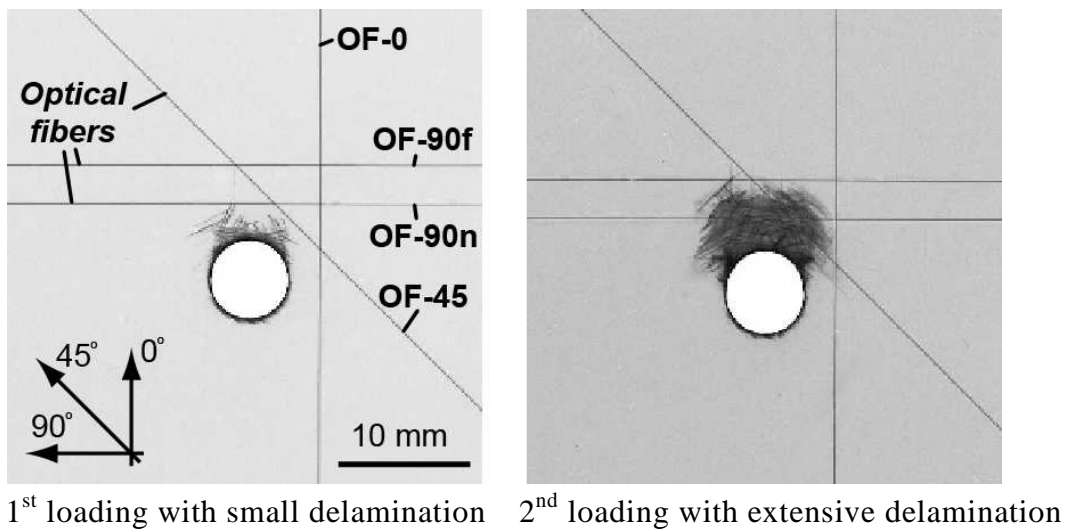


Fig. 26 Experimental setup of Mode I crack growth test in foam-core CFRP facesheet sandwich structure with a crack arrester



(a) Schematic view of embedded optical fiber in CFRP laminates



(b) Soft X-ray images of embedded optical fibers and damages

Fig. 27 Embedded optical fiber for damage sensing in CFRP laminates

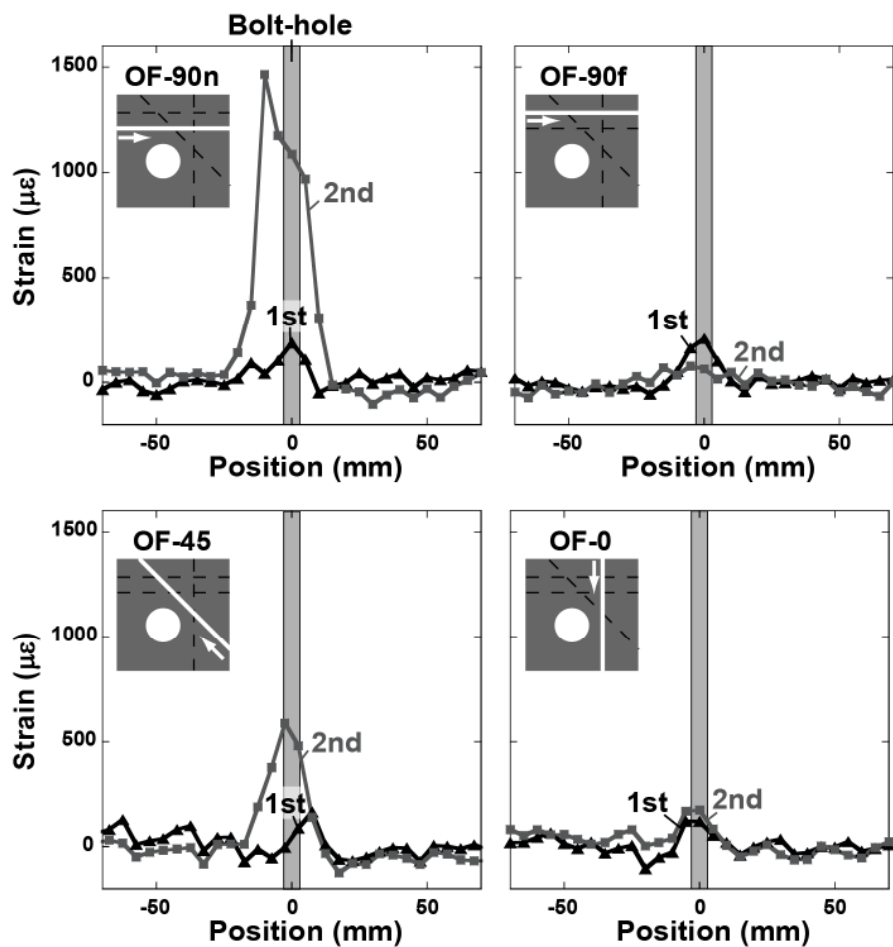


Fig. 28 Change in Strain distribution around the bolt hole due to damages

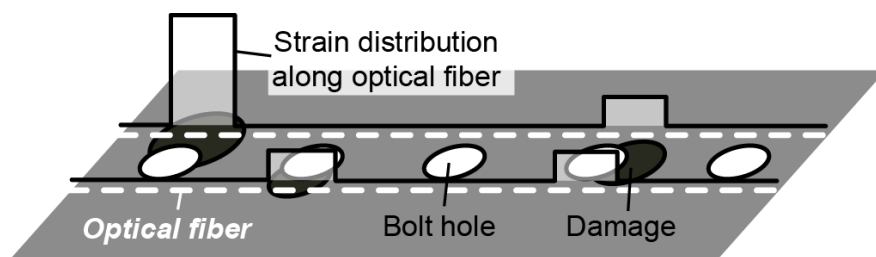


Fig. 29 Proposed damage detection system using BOCDA distributed strain monitoring

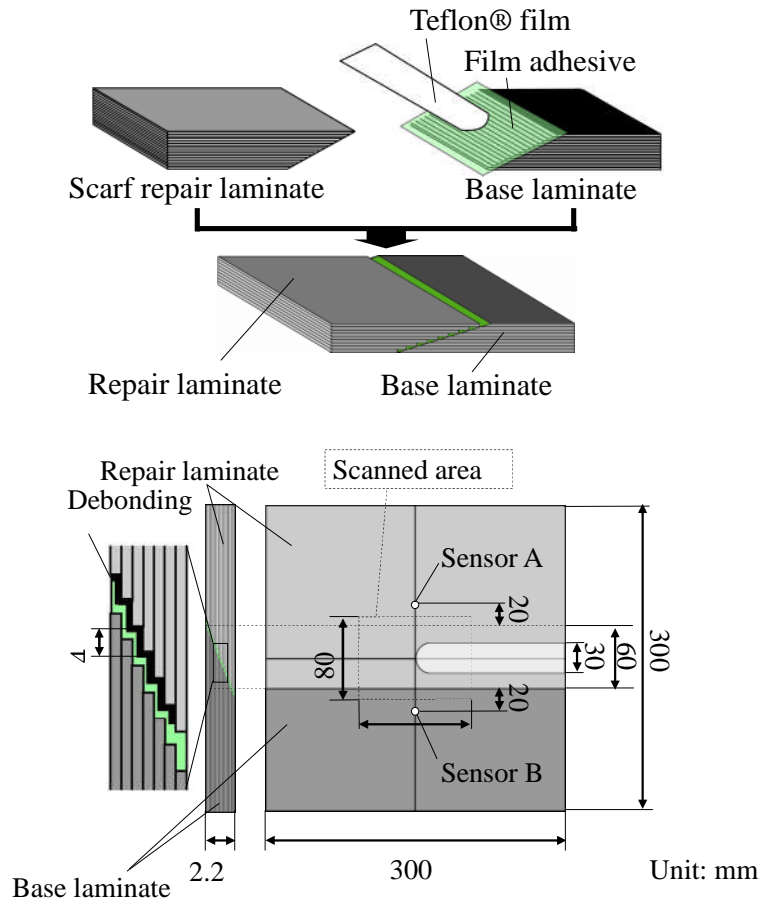


Fig. 30 Schematic diagram of the scarf repaired specimen, laser scanned area and position of the AE sensor

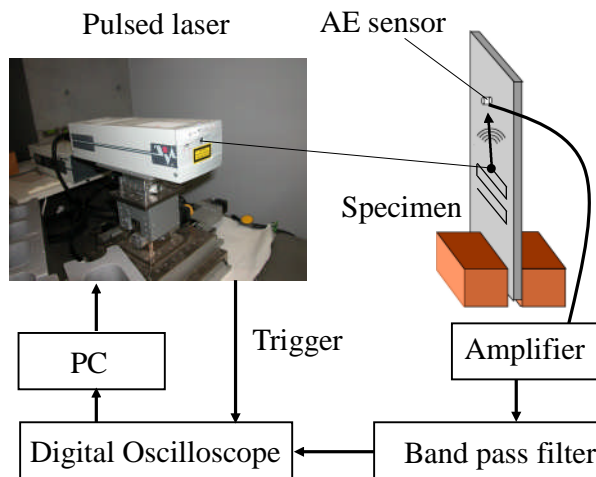
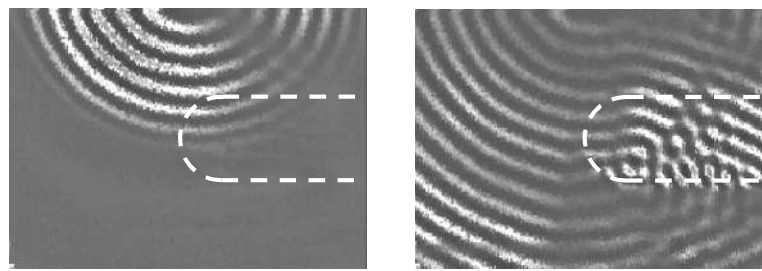


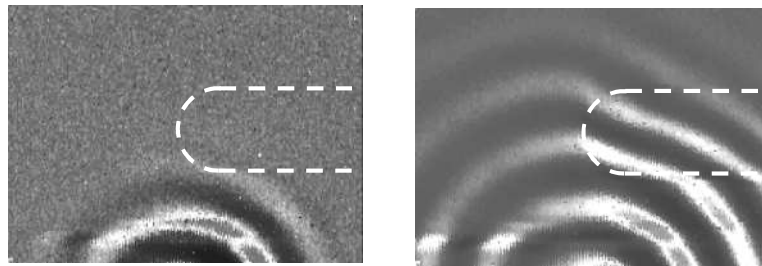
Fig. 31 Schematic diagram of the ultrasonic wave visualization technique



$t = 40\mu\text{s}$

$t = 80\mu\text{s}$

(a) BPF of 200kHz, Sensor A

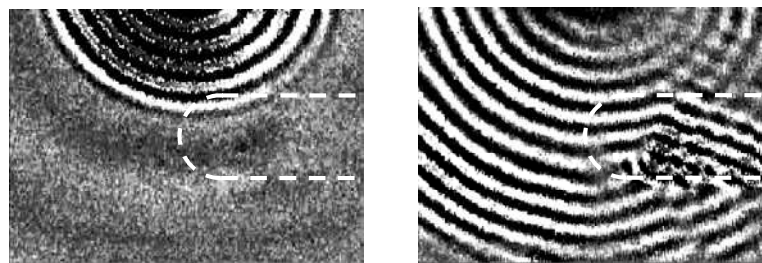


$t = 40\mu\text{s}$

$t = 80\mu\text{s}$

(b) BPF of 50kHz, Sensor B

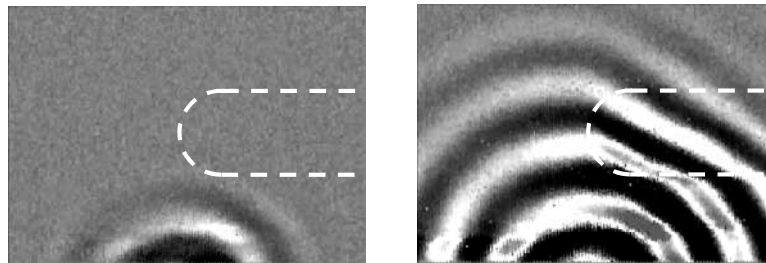
Fig. 32 Visualized results in the scarf repaired specimen before coating



$t = 40\mu\text{s}$

$t = 80\mu\text{s}$

(a) BPF of 200kHz, Sensor A



$t = 40\mu\text{s}$

$t = 80\mu\text{s}$

(b) BPF of 50kHz, Sensor B

Fig. 33 Visualized results in the scarf repaired specimen after coating.

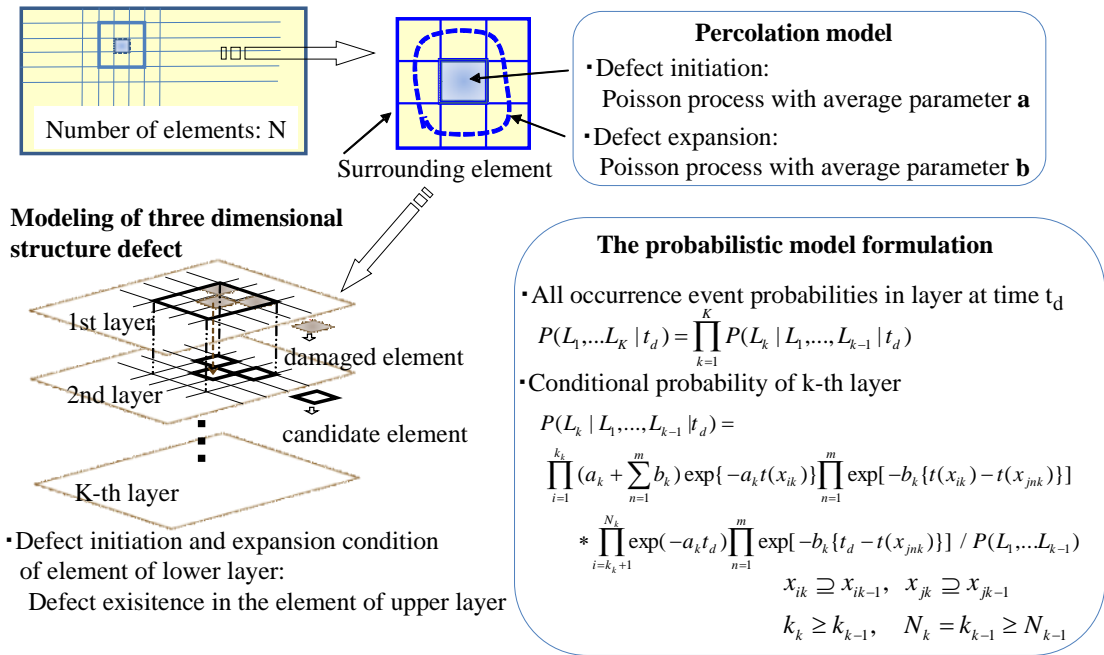


Fig. 34 Structural defect model to consider spatial correlation and time dependence based on three dimensional percolation method

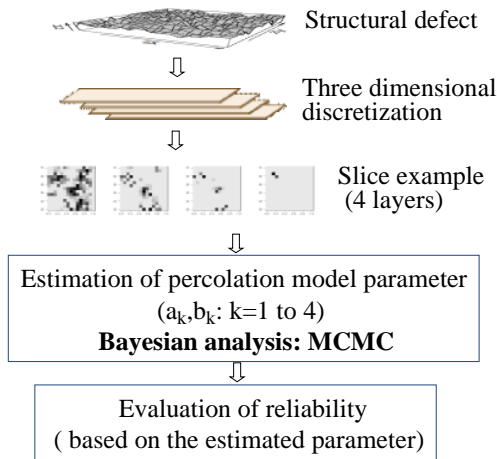


Fig. 35 Outline flow of reliability assessment

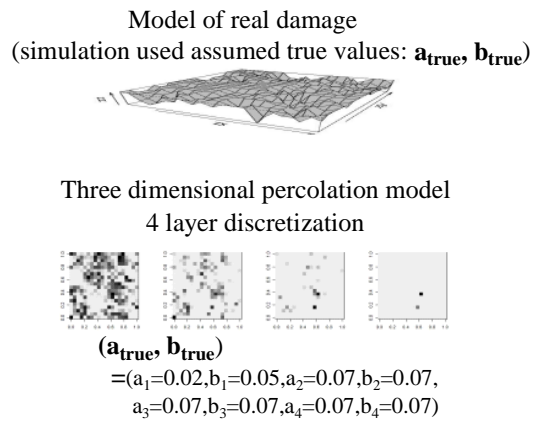


Fig. 36 Numerical example

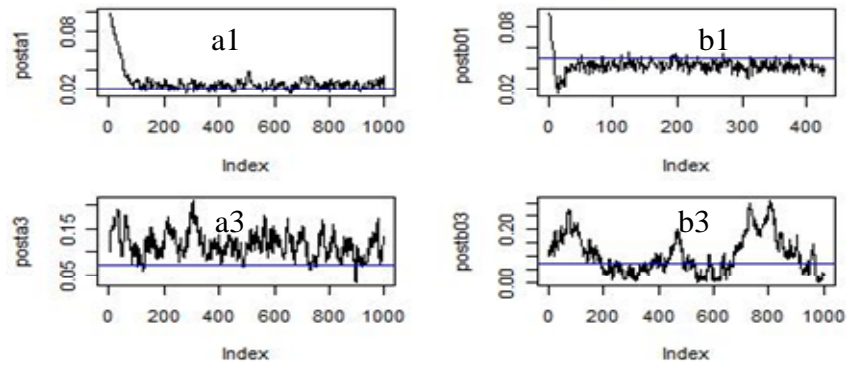


Fig. 37 Process of generation of MCMC unknown population parameter (defect initiation and expansion parameters)

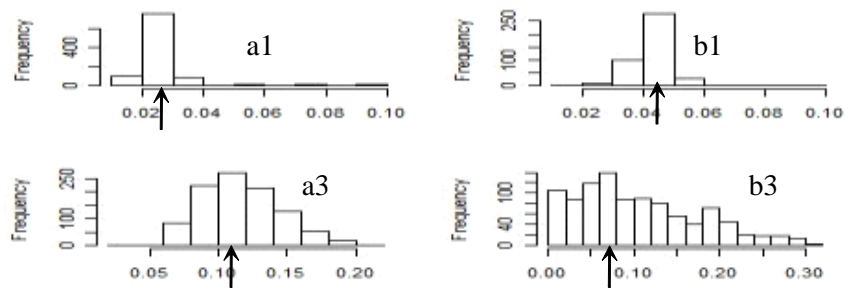


Fig. 38 Posterior probability distribution function of defect parameters



Fig. 39 Maiden flights of XP-1 and XC-2



Fig. 40 Full scale static test airframe and loading fixture of XP-1

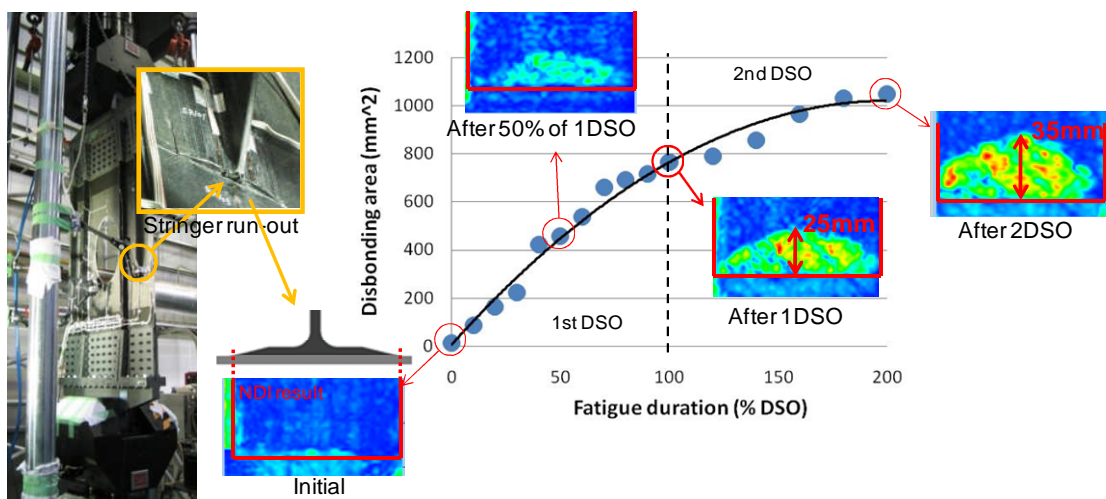


Fig. 41 Sub-component test and slow growth of stringer run-out disbonding



Fig. 42 Full-scale wing box ultimate load test

Table 4 Number of Accident by Type of Aircraft

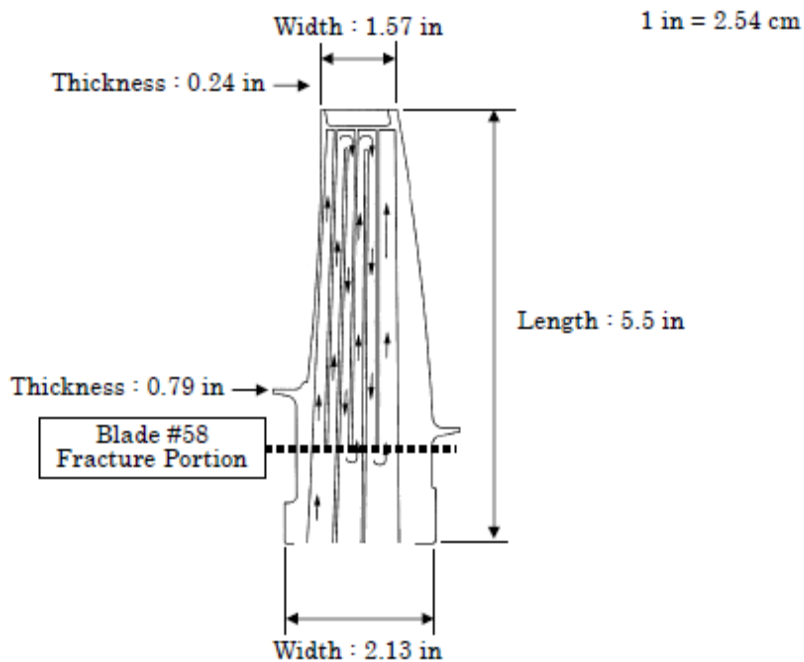
| Aircraft \ Year | Large Airplane | Small Airplane | Rotorcraft | Glider, ULP or other | Total |
|-----------------|----------------|----------------|------------|----------------------|-------|
| 2009 | 6 | 2 | 7 | 4 | 19 |
| 2010 | 0 | 4 | 4 | 4 | 12 |

Table 5 Number of Serious Incident by Type of Aircraft

| Aircraft \ Year | Large Airplane | Small Airplane | Rotorcraft | Glider, ULP or other | Total |
|-----------------|----------------|----------------|------------|----------------------|-------|
| 2009 | 4 | 5 | 2 | 0 | 11 |
| 2010 | 7 | 1 | 1 | 3 | 12 |

ULP: Ultra Light Plane

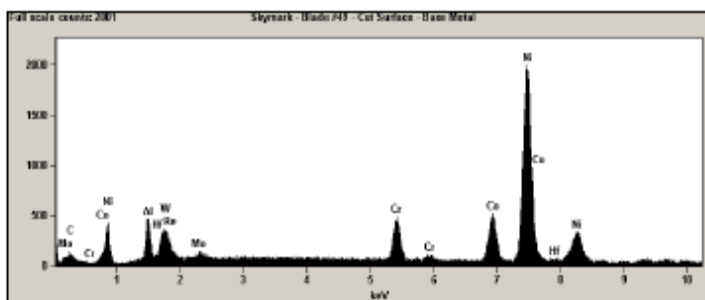
Part Number : 1881M52G05



Base Metal Spectrum - DSR142

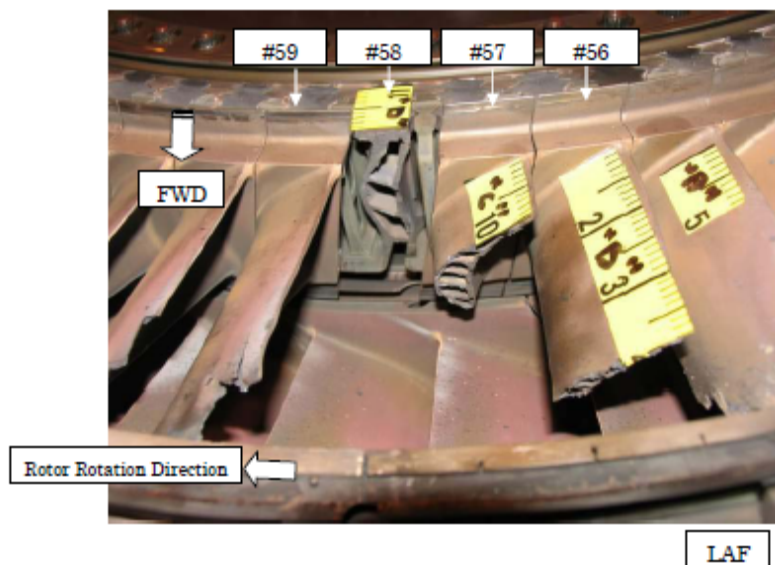
Materials :

- Nickel (Ni)
- Cobalt (Co)
- Chrome (Cr)
- Hafnium (Hf)
- Aluminum (Al)
- Tungsten (W)
- Rhenium (Re)



From Engine Manufacturer's Document

Fig. 43 HPT Stage 2 blade



Over View

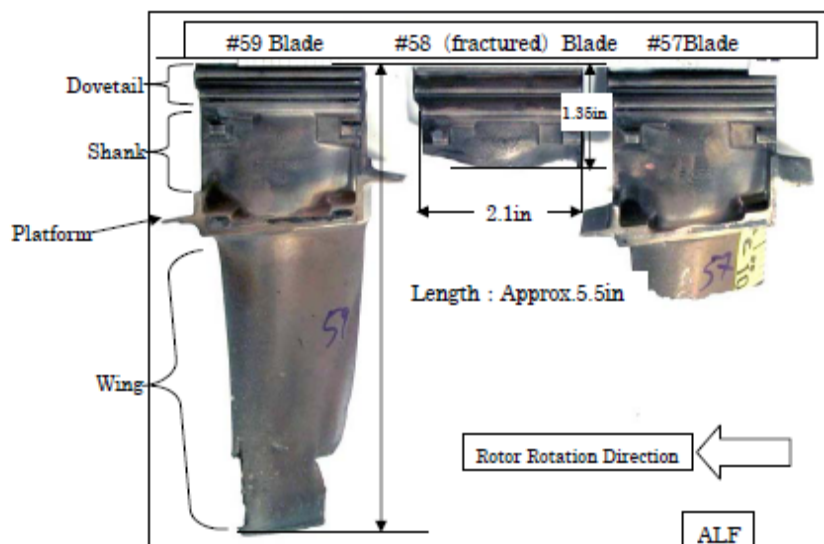


Fig. 44 Stage 2 HPT shank separation and adjacent blade damage

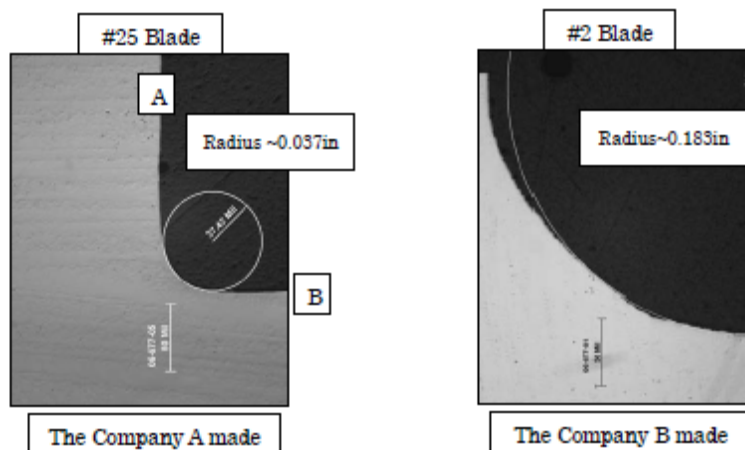
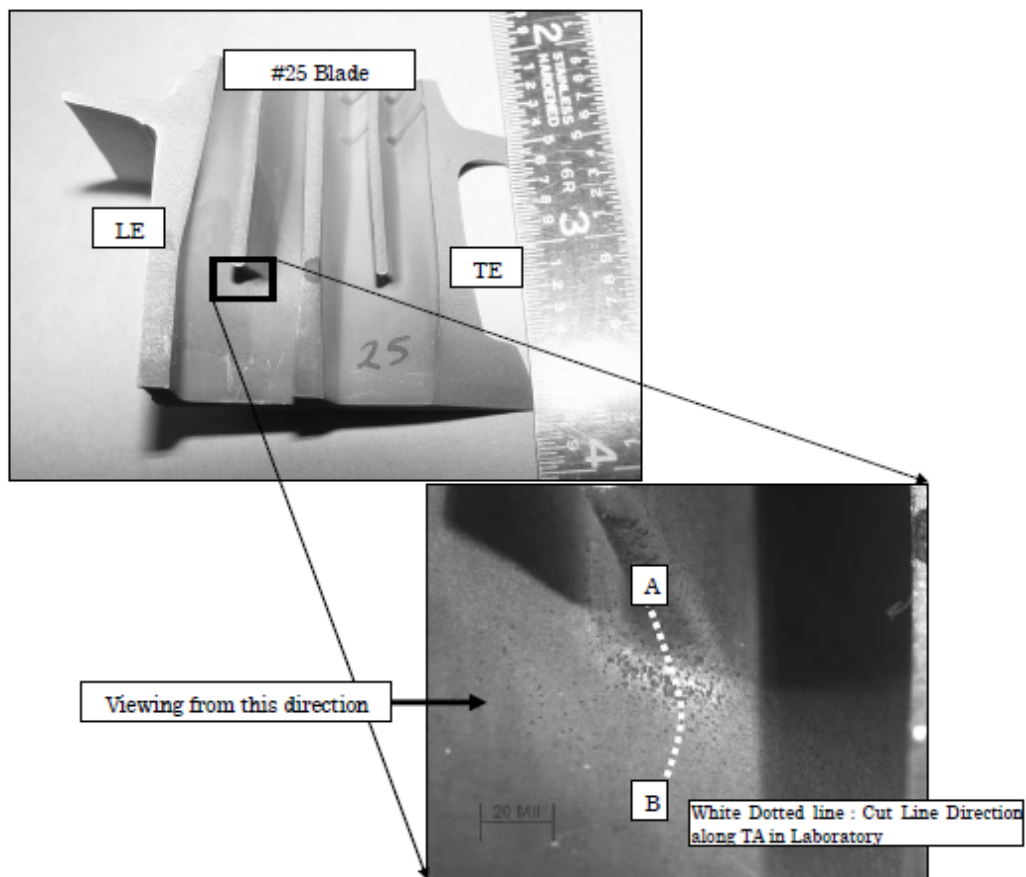
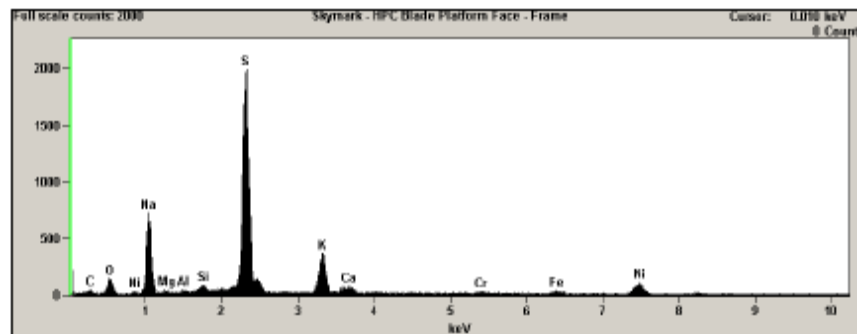
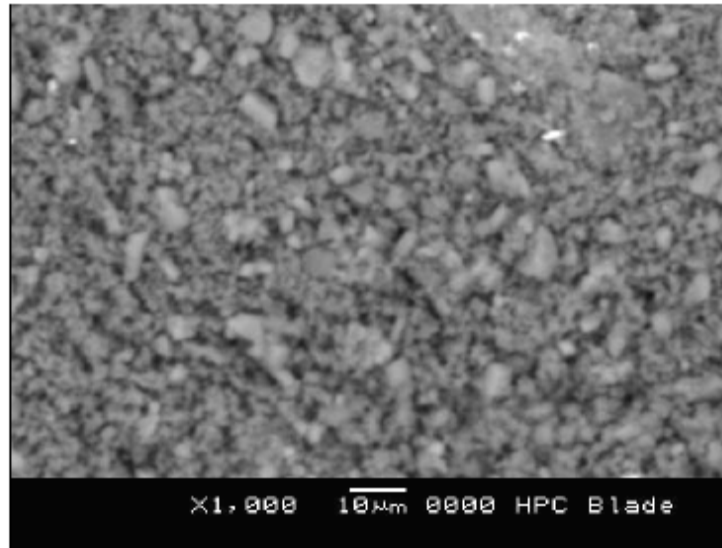
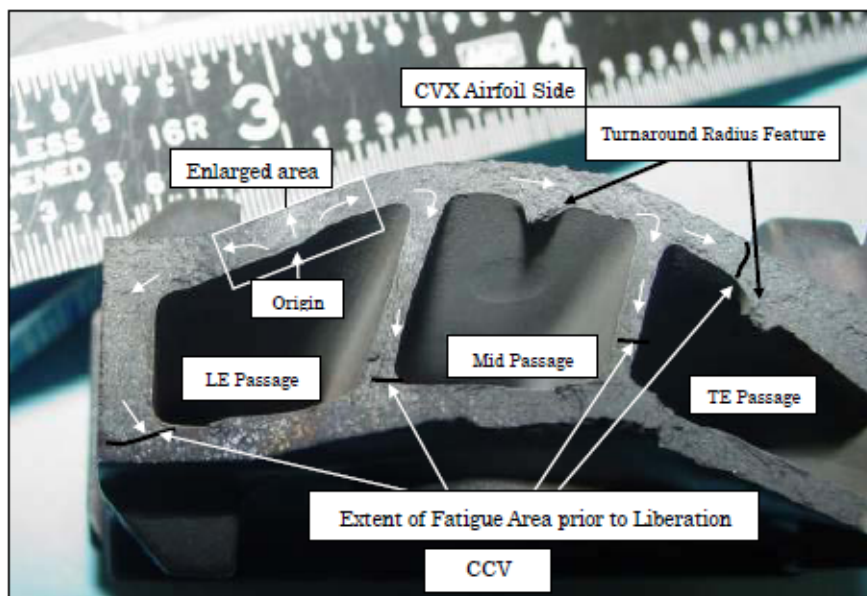


Fig. 45 Differences of turnaround radius features



White Debris Exhibited Elevated Sulfur(S), Sodium(Na)
and Potassium(K) along with Oxygen(O)

Fig. 46 Debris from Stage 10 HPC blades



Fracture Origin Region (Enlarged Area)

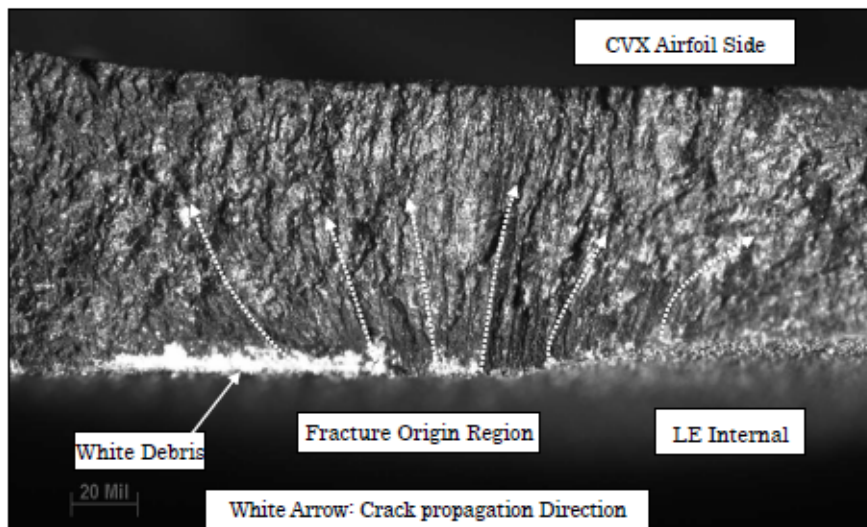


Fig. 47 Fracture origin of #58 blade and internal cooling air passage